# $CO_2$ Conversion in Non-Uniform Discharges: Disentangling Dissociation and Recombination Mechanisms

A.J. Wolf,[†,‡] F.J.J. Peeters,[*,†,‡] P.W.C. Groen,[‡] W.A. Bongers,[‡] and M.C.M van de Sanden[*,‡,¶]

†*Contributed equally to this work*

‡*DIFFER, De Zaale 20, 5612AJ Eindhoven, The Netherlands*

¶*Dept. of Applied Physics, Plasma Materials Processing group, Eindhoven University of Technology, PO Box 513, 5600MB Eindhoven, The Netherlands*

E-mail: f.j.j.peeters@differ.nl; m.c.m.vandesanden@differ.nl

**Abstract**

Motivated by environmental applications such as synthetic fuel synthesis, plasma-driven conversion shows promise for efficient and scalable gas-conversion of $CO_2$ to CO. Both discharge contraction and turbulent transport have a significant impact on the plasma processing conditions, but are, nevertheless, poorly understood. This work combines experiments and modeling to investigate how these aspects influence the CO production and destruction mechanisms in the vortex-stabilized $CO_2$ microwave plasma reactor. For this, a 2D axisymmetric tubular chemical kinetics model of the reactor is developed, with careful consideration for the non-uniform nature of the plasma and the vortex-induced radial turbulent transport.

Energy efficiency and conversion of the dissociation process show a good agreement with the numerical results over a broad pressure range from 80-600 mbar. The occurrence of an energy efficiency peak between 100-200 mbar is associated with a discharge mode transition. The net CO production rate is inhibited at low pressure by the plasma temperature, while recombination of CO to $CO_2$ dominates at high pressure. Turbulence-induced cooling and dilution of plasma products limit the extent of the latter. The maxima in energy efficiency observed experimentally around 40 % are related to limits imposed by production and recombination processes. Based on these insights, feasible approaches for optimization of the plasma dissociation process are discussed.

# Introduction

Plasma technology has proven useful in various gas conversion and processing applications on industrial scale,[1,2] including high-temperature plasma pyrolysis of toxic gasses and ozone production. In light of emerging environmental challenges in recent decades, plasma technology is also being considered for the conversion of small but stable molecules, including $N_2$ and $CO_2$, for applications such as efficient nitrogen fixation (to improve on the Haber-Bosch process) or $CO_2$ utilization as feedstock in industrial and chemical processes.[3] The economic viability of large scale deployment of such processes depends heavily on the extent to which performance parameters such as energy efficiency, selectivity, and yield can be optimized. Here, plasmas provide the opportunity to readily achieve processing conditions which are otherwise unattainable in conventional chemical processes. In particular the high power density (which benefits process intensity) and the non-equilibrium characteristics of plasmas may be exploited for selective activation of specific, more efficient, reaction channels.[4,5]

Plasma-driven activation of $CO_2$ shows great promise for the efficient production of CO feedstock for energy-dense synthetic fuels[6,7] and other carbon-based chemicals. Early plasma-chemistry studies on $CO_2$ conversion by Legasov et al.[8] report promising efficiency

values of 80 % with a conversion of 25-20 % in steady state microwave plasmas under subsonic flow conditions. At the time of publication, the high experimental energy efficiency values were explained by a mechanism of vibrational dissociation. This non-thermal process leverages the non-equilibrium characteristics of the discharge in such a way that the electron energy is preferentially transferred to the vibrational excitation of the $CO_2$ molecules.[4] Such conditions of high vibrational temperature and a low translational temperature were later supported by several in-situ temperature measurements in the plasma.[9] The fundamental reaction mechanisms, however, remain a topic of dispute. Recent attempts to reproduce the non-equilibrium conditions have consistently resulted in high (gas) temperatures under otherwise similar operational conditions. Rayleigh scattering measurements of the central plasma temperature reveal that 3000-5000 K is readily achieved under steady state conditions.[10] Such temperature values are known to induce thermal decomposition of $CO_2$, and therefore rule out a significant contribution of vibrational dissociation. Under the high-temperature conditions, energy efficiency values of up 50 % have been reported (at a conversion of 10 %)[10] and conversion values up to 80 % (at an energy efficiency of 25 %).[11] Generally, the highest energy efficiencies are typically reached at somewhat lower conversions, and vice versa. The record energy efficiencies of 80 % previously associated with the vibrational dissociation mechanism have not been reproduced in the recent surge of experiments.[10–17]

Apart from processing conditions inside the plasma, the plasma surroundings impact the overall process efficiency to a similar extent. The cooling trajectory of dissociated products, which occurs in the gas layers surrounding the plasma and further downstream in the effluent, strongly influences the extent to which plasma products are retained.[10,18–21] A temperature of over 2000 K in the afterglow is known to promote CO recombination reactions. In order to minimize such losses following plasma conversion at 3000 K or higher, cooling rates of at least $10^6$ K/s are required to cool the plasma products below 2000 K sufficiently fast.[10,22] Furthermore, the post-discharge kinetics involving atomic oxygen radicals may facilitate additional CO production in the plasma afterglow by means of the $CO_2 + O \rightarrow CO + O_2$ reaction.[23] This reaction channel may facilitate substantial efficiency increases, with simulations indicating in particular optimized conditions an increase in energy efficiency from 47 % to 86 %.[24]

Two important yet often poorly considered aspects of influence to both the plasma conditions and its surroundings are non-uniform heating (which is associated with discharge contraction at moderate to high pressure conditions) and the transport effects induced by plasma-flow interaction. As these phenomena promote highly non-homogeneous processing conditions, localized regions of dominant production and recombination may occur. Identification and quantification of the local contributions of CO production and recombination is essential to understand and further optimize the overall reactor performance.

Non-uniform power deposition is common in plasma reactors, as the power deposition tends to concentrate at elevated pressures due to discharge contraction effects.[25] In $CO_2$ plasmas, discharge contraction occurs in distinct stages or discharge modes with rising pressure, which results in strong pressure dependence of both power density and gas temperature.[26] The two prevalent discharge modes in the pressure range from 100 mbar to atmospheric conditions are the L-mode and H-mode plasmas, characterized visually by their different extent of radial constriction as shown in Fig. 1a and b, respectively. In comparison to homogeneous heating conditions, the effects of non-uniformity and transport can considerably influence the local discharge and post-discharge processing conditions, as illustrated in Fig. 2. Furthermore, discharge contraction in flow reactors results in a partial processing of the gas flow, i.e. the gas flow may partly bypass the plasma, as in its contracted state the radial plasma dimension is typically much smaller than the reactor tube. Partial gas processing is believed to contribute to the relatively low conversion degrees, for instance in gliding arc plasmas.[15]

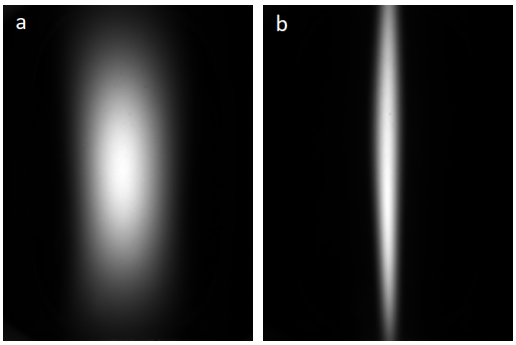


Figure 1: The effect of discharge contraction on the $CO_2$ microwave plasma leads to distinct discharge modes: (a) an L-mode plasma at 100 mbar and (b) an H-mode plasma at 250 mbar. The horizontal and vertical dimension of the images corresponds to, respectively, the discharge tube diameter and the section of tube intersecting the microwave cavity.

Vortex flows are commonly employed for the purpose of plasma-stabilization.[27] Deviations from laminar gas flows in vortex-stabilized plasma reactors can further impact the transport in and around the plasma. The CFD simulations in Fig. 3 show clear deviations from laminar flow due to the formation of advective recirculation cells. Such flow structures are known to enhance the axial flow velocity near the reactor wall[28] which, compared to a developed laminar flow, may lead to an increased gas bypass around contracted discharges. In addition, turbulence induced at the plasma edge may enhance radial transport of heat and particles and influence plasma parameters such as gas temperature.[29] Moreover, the enhanced lateral (turbulent) transport between the central and peripheral regions of vortex flows[30] can result in a shifted location of quenching from the axially downstream location (in case of homogeneous processing) to a region laterally around the plasma (Fig. 2). These po-

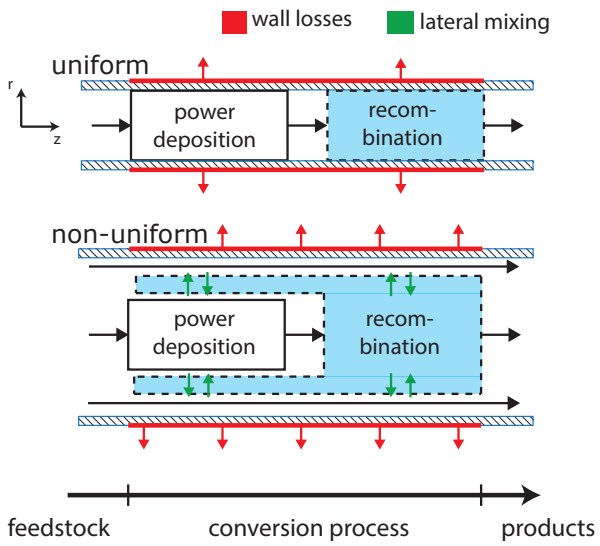


Figure 2: Illustration of the distinction processing conditions in a plasma flow reactor between scenarios of uniform and non-uniform power deposition. Indicated are the region of power deposition in which in which endothermic processes are driven, and the surrounding quenching zone in which product recombination may occur.

tential implications of the gas-flow dynamics on gas bypass, plasma conditions and quenching conditions illustrates the importance of considering vortex-induced transport effects on the plasma conversion process.

Reactor models of $CO_2$ plasma often fail to capture the non-uniform heating and transport effects related to the 3-dimensional flow. In general, full 3D flow implementations remain too computationally expensive, especially when combined with chemical and charged-particle kinetics in the plasma.[31] Therefore, numerical work is often limited to 0D global models[10,32] or plug flow reactors with heat transfer to the walls.[17,33] Recently, the plug flow model has been extended to successfully capture basic radial transport by the addition of a concentrically surrounding outer volume.[34] This approach however still lacks consideration of vortex-enhanced turbulence effects.

This work employs a 2D axisymmetric tubular flow geometry with 25 concentric volume elements to capture the axial and radial variations in composition and temperature induced by non-uniform heating and gas-dynamic transport. The model uses only a minimal set of input parameters and does not contain computationally intensive, and physically complicated, self-consistent models. Species transport is considered in simplified form by assuming advective transport only in the axial direction and turbulence-enhanced diffusive transport only in the radial direction. Here, the vortex flow dynamics are captured by describing its effect on radial transport by an effective radial transport parameter. A basic set of neutral chemical reactions are incorporated in the model while vibrational kinetics are disregarded,

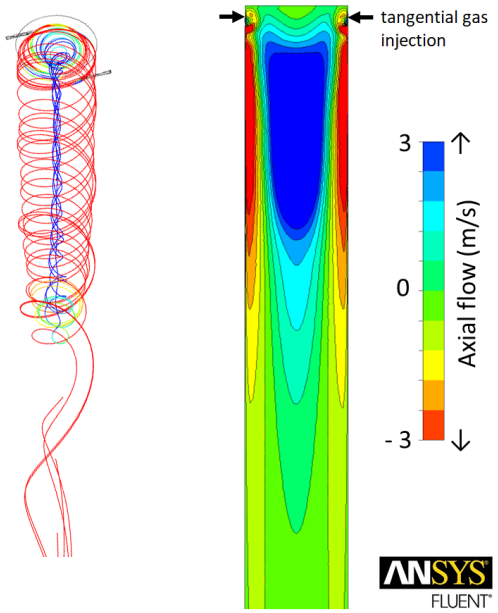


Figure 3: CFD simulation of the vortex flow related to the experiments presented in this work. Color indicates the axially directed advective velocity component. Left: 3D rendering of streamlines. Right: Axial cross section

i.e. the plasma functionally acts as a heat source. This choice is motivated by recent experimental and numerical studies which show that, despite the fact that the microwave field energy is largely coupled to vibrational modes of $CO_2$, thermal dissociation prevails over vibrational dissociation due to strong VT-relaxation under realistic moderate-to atmospheric discharge conditions.[16,17]

This work assesses the effects of conversion and recombination processes on the energy efficiency by combined experiments and modeling. Here, we build on our previous work[25,26] in which the $CO_2$ microwave discharge is characterized in terms of gas temperature and power density profile. The model results are used to evaluate the contributions of production and recombination to the overall $CO_2$ conversion process. Finally, the limitations and opportunities of plasma-conversion in $CO_2$ microwave plasmas are discussed, and an outlook is provided.

# Experimental Setup

The plasma conversion experiments are carried out in a vortex-stabilized microwave reactor in a configuration commonly used for $CO_2$ conversion.[8,10,11] The source consists of a 2.45 GHz magnetron with a CW power output set at 1000 W. The microwaves are applied to the $CO_2$ flow as a $TE_{10}$ standing wave mode in a WR340 rectangular waveguide, as illustrated in

Fig. 4. The gas flow is injected tangentially into the quartz tube, generating a swirling flow for the purpose of lateral plasma stabilization in the center of the discharge tube. This prevents high heat loads to the walls. The flow rate is regulated by mass flow controllers at the inlets, while the reactor chamber pressure is regulated by a throttle valve, situated downstream between process and vacuum pump. The impedance of the plasma is matched to the source by means of a 3-stub impedance tuner which keeps the reflected power below 1 %. This allows for stable operating conditions at flow rates ranging from 2-28 slm and a pressure range between 50 mbar and atmospheric pressure. The absorbed power, which is determined from the difference in forward and reflected power, is measured by calibrated directional couplers. In more recent experiments a six-port reflectometer integrated in the impedance-matching system (HOMER S-TEAM STHT2450) is also employed, providing superior accuracy in the absorbed power measurement. Further details about the present source and tuning configuration have been described previously.[11,25]

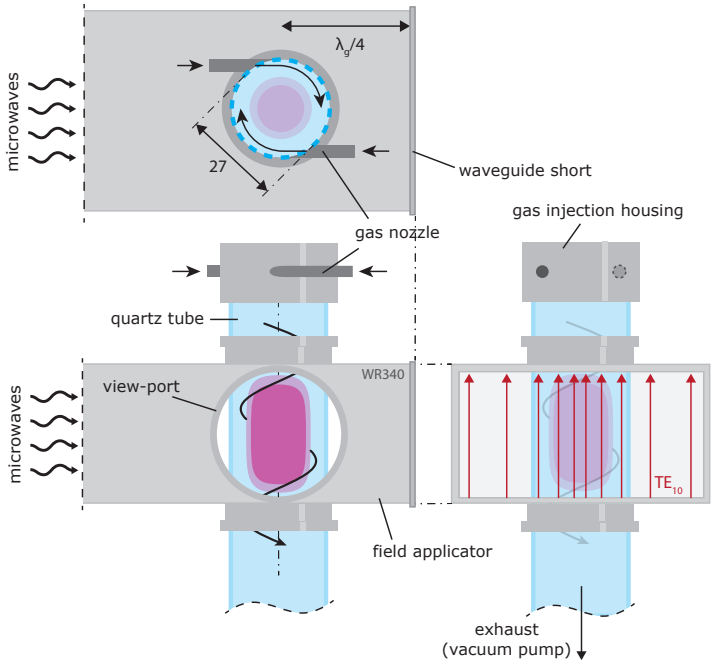


Figure 4: Illustration of the field applicator and the flow geometry.

Gas temperature values $T_{\mathrm{gas}}$ in the center of the discharge are obtained via a Doppler broadening measurement of the $\mathrm{O}(3\mathrm{s}^5\mathrm{S}^0 \leftarrow 3\mathrm{p}^5\mathrm{P})$ oxygen line at 777 nm.[25,26] The conversion of $CO_2$ ($\alpha$) and the energy efficiency ($\eta$) are the two main global performance metrics of the dissociation process. Here, $\alpha$ is defined according to the stoichiometric ratios of the reduction reaction, $\mathrm{CO_2} \rightarrow (1-\alpha)\mathrm{CO_2} + \alpha\mathrm{CO} + \frac{\alpha}{2}\mathrm{O_2}$, and can be written in terms of the

molar fractions $\chi_i$ of the species $i$ in the dissociated mixture,

$$\alpha = \frac{\chi_{\mathrm{CO}}}{\chi_{\mathrm{CO}} + \chi_{\mathrm{CO_2}}}. \tag{1}$$

The energy efficiency $\eta$ of the dissociation process is defined based on the enthalpy $\Delta H_{\mathrm{f}}^{\ominus} = 2.93\,\mathrm{eV}$ of the net dissociation process ($\mathrm{CO_2} \rightarrow \mathrm{CO} + \frac{1}{2}\mathrm{O_2}$), and can be expressed in terms of the produced CO particle flux $\Gamma_{\mathrm{CO}}$ and the total input power $P_{\mathrm{abs}}$ or the average energy expenditure per produced CO molecule ($\mathcal{E}_{\mathrm{CO}}$):

$$\eta = \frac{\Gamma_{\mathrm{CO}} \cdot \Delta H_{\mathrm{f}}^{\ominus}}{P_{\mathrm{abs}}} = \frac{\Delta H_{\mathrm{f}}^{\ominus}}{\mathcal{E}_{\mathrm{CO}}} \tag{2}$$

Combining the previous expressions and introducing a global (average) specific energy input (SEI) in the reactor ($\mathcal{E}_\nu$), the efficiency may be expressed in terms of the conversion

$$\eta = \alpha \cdot \frac{\Delta H_{\mathrm{f}}^{\ominus}}{\mathcal{E}_\nu}\,, \tag{3}$$

The conversion $\alpha$ is determined from the mole fractions $\chi_i$ of the main species in the reactor effluent, which are measured by means of mass spectrometry analysis (HIDEN HAL RC201 QIC) in the cooled and stabilized reactor output flow sufficiently far from the heat source.

# Model

The chemical reactor model geometry constitutes a long cylindrical tube with constant diameter, discretized into 25 concentrically nested cylindrical volume elements of equal thickness. Each cylindrical volume element $j$ carries a mass flow $\dot{m}_j$ from $z = 0$ to $z = L$ with a velocity in the $z$-direction given by:

$$v_j = \frac{\dot{m}}{A_j \overline{M}_j n_{0,j}(p, T_j)}\,, \tag{4}$$

with $\overline{M}_j$ the mean molar mass, $A_j$ the cross-sectional surface area of a volume element and $n_{0,j}(p, T_j)$ the local neutral density. For clarity of presentation, the functional dependence on $z$ is omitted in all variables. In the radial direction, exchange of particles between the concentric volume elements is described by Fickian diffusion:

$$\Gamma^i_{j,j+1} = -n_{0,j}(p, T_j) D_{\mathrm{eff},j} \frac{\Delta \chi^i_{j,j+1}}{\Delta R^i_{j,j+1}}\,, \tag{5}$$

where $\Gamma^i_{j,j+1}$ is the particle flux of species $i$ through the surface between volume element $j$ and $j+1$, $D_{\mathrm{eff},j}$ is an effective diffusion coefficient (assumed equal for all species $i$), $\Delta\chi^i_{j,j+1}$ is the difference in molar fraction of species $i$ between the volume elements and $\Delta R^i_{j,j+1}$ is the difference in radial center positions between volume elements. Here, a positive value of $\Gamma^i_{j,j+1}$ indicates a net outwards flux of species i and vice versa. Similarly, the radial heat conduction is described by the heat flux density

$$q_{j,j+1} = \lambda_{\mathrm{eff},j}\frac{\Delta T_{j,j+1}}{\Delta R_{j,j+1}}, \tag{6}$$

with $\lambda_{\mathrm{eff},j}$ the effective thermal conductivity of the gas mixture and $\Delta T_{j,j+1}$ the temperature difference between volume element $j$ and $j+1$. The effective diffusion coefficient $D_{\mathrm{eff},j}$ and effective heat conductivity $\lambda_{\mathrm{eff},j}$ are the summations of laminar and turbulent components

$$D_{\mathrm{eff},j} = D_{\mathrm{L},j} + D_{\mathrm{T},j} = 1.0\times10^{-4}\frac{{T_j}^{3/2}}{p} + \frac{\nu_{\mathrm{T},j}}{Sc_{\mathrm{T}}} \text{ and} \tag{7}$$

$$\lambda_{\mathrm{eff},j} = \lambda_{\mathrm{L},j} + \lambda_{\mathrm{T},j} = 2.5\times10^{-3}\frac{T_j^{3/2}}{T_j+300} + C_{p,j}\frac{\nu_{\mathrm{T},j}}{Pr_{\mathrm{T}}}\,, \tag{8}$$

where the laminar diffusion coefficient and heat conductivity $D_{\mathrm{L},j}$ and $\lambda_{\mathrm{L},j}$ are approximated by functions of $T$ and $p$ without distinguishing between different species or mixture compositions. The chosen functions are fits to the average diffusion coefficient and thermal conductivity for an 80 % $CO_2$, 10 % CO, 10 % $O_2$ mixture. The turbulent contributions, $D_{\mathrm{T},j}$ and $\lambda_{\mathrm{T},j}$ depend on the turbulent viscosity $\nu_{\mathrm{T},j}$ and the local heat capacity $C_{p,j}$ in $\mathrm{Jmol^{-1}K^{-1}}$. The turbulent Schmidt number $Sc_{\mathrm{T}}$ and the turbulent Prandtl number $Pr_{\mathrm{T}}$ are constants for which standard CFD simulation values of 0.71 and 0.85, respectively, are used. Approximating $D_{\mathrm{L},j}$ and $\lambda_{\mathrm{L},j}$ with species- or mixture-independent functions greatly simplifies calculations with a limited effect on model results, since the turbulent terms are generally more than an order of magnitude greater than the laminar terms. The only transport parameter not directly solved for in the model is the turbulent viscosity $\nu_{\mathrm{T},j}$. This parameter can be expected to vary strongly with position because of the strong influence of composition and temperature. CFD simulations of the vortex flow (which includes a heat source representing the plasma) in ANSYS Fluent© show that the radial variation in $\nu_{\mathrm{T}}$ can be approximated by a quadratic function in $r$, while the axial variation decays only gradually at axial positions downstream from the heat source, i.e. the plasma position. Since initial results of the model suggest that both turbulent mixing of species and temperature occurs in the region surrounding the plasma, with nearly uniform distributions of species fractions and temperature at positions downstream of the high temperature zone, the turbulent viscosity can be represented well by

$$\nu_{\mathrm{T},j} = \nu_{\mathrm{T},peak} \cdot \left(1 - \frac{R_j^2}{R_{\mathrm{tube}}^2}\right) , \tag{9}$$

which reduces the number of input parameters required to characterize radial transport in the reactor to a single value: $\nu_{\mathrm{T},peak}$.

The 3D CFD simulations using a $k-\epsilon$ model of the vortex flow in Fig. 3 show that the radial distribution of axial mass flow $\dot{m}(r)$ may vary significantly as a function of the radial position $r$. Despite this, radial variations on the mass flow distribution via $\dot{m}_j$ are found to have only a minor impact on the model outcome. The radial distribution of mass flow rate is, therefore, approximated by a constant function so that

$$\dot{m}_j = \dot{m}\frac{A_j}{\pi R_{tube}^2} , \tag{10}$$

with $\dot{m} \propto \Phi_{CO_2}$ the total mass flow at the input of the reactor. We note that, as a consequence of this simplification, vortex-induced advective recirculating flow cells (such as observed in the CFD simulation in Fig. 3 by the region of on-axis upward flow) is disregarded. The disregard of these flow cells for the sake of simplicity is justified by the fact that the strongest gradients in temperature and species distribution occur around the plasma, while at the same position the species and energy transport is accounted for mostly by turbulent mixing in the radial direction rather than axial advective transport. As will become apparent, advective transport may dominate over radial diffusive transport at low pressures, but in those cases heating of the gas stream occurs almost uniformly across the width of the tube due to effective radial transport. Therefore the detailed shape of the advective flow field remains irrelevant in first approximation (i.e. at low pressure, a 1D model could describe the reactor with sufficient accuracy, so that results depend only on the total mass flow rate $\dot{m}$).

The spatial distribution of power deposition over the volume elements $P_{\mathrm{V},j}$ is obtained from images of spontaneous emission of the $\mathrm{O}(3\mathrm{s}^5\mathrm{S}^0 \leftarrow 3\mathrm{p}^5\mathrm{P})$ triplet at 777 nm, following previously described methodology.[26] The images are inversely Abel transformed to obtain radially resolved emission intensity profiles. A linear relation is assumed between electron density and power density as described by Joule heating. Gaussian functions are fitted to the emission intensity profile in both $r$- and $z$-directions, with the resulting power density function integrated over the width of each volume element to obtain functions in $z$ only. Power deposition is assumed to lead to direct gas heating, i.e. thermalization of the heavy particle temperatures is assumed. For this reason, non-equilibrium vibrational kinetics are omitted in the calculations. These assumptions are justified by previous work which shows that, despite substantial preferential vibrational excitation, fast thermalization occurs on timescales below 100 µs[16] and the thermal conversion mechanisms dominate over vibrational mechanisms under steady state and high temperature reactor conditions.[17]

In total 26 reactions between the 5 most prevalent neutral chemical species in the plasma ($CO_2$, CO, $O_2$, O, C) are incorporated in the model. The chemical mechanism is based on the chemical reaction rates from Butylkin et al.[22] with supplementary reactions involving atomic carbon from Beuthe et al.[35] and can be found in the Supporting Information of this article. The contribution of electron-impact driven chemical reactions was investigated in the model by including an electron density proportional to the power density $P_{\mathrm{V},j}$ at each point, based on electron density values obtained previously.[25] It was found that electron-impact dissociation reactions of $CO_2$, CO and $O_2$, with effective rate coefficients obtained from a global model of the high temperature kinetics currently in preparation, contribute at most 10% to the total CO flux at the output of the reactor. To simplify the discussion, the effect of electron-impact reactions will be neglected for the remainder of this work.

Energy not converted to CO and $O_2$ leaves the reactor as heat, either via convection or radiation at the outer wall of the reactor, described by the boundary condition

$$q_{wall} = \omega(T_J - T_{\mathrm{env}}) + \epsilon\sigma_{\mathrm{SB}}(T_J^4 - T_{\mathrm{env}}^4)\,. \tag{11}$$

Here, $T_{\mathrm{J}}$ the temperature of the gas in the outermost volume element, $T_{\mathrm{env}}$ the temperature of the environment fixed at 300 K, $\omega$ a heat transfer coefficient fixed at 25 $\mathrm{W/m^2K}$ (a typical value for forced convection of air around the tube), $\epsilon$ the emissivity of quartz fixed at 0.93 and $\sigma_{\mathrm{SB}}$ the Stefan-Boltzmann constant. All governing equations in the model, including the continuity equations and thermodynamic functions not discussed here, are described by Eqs. S1-S23 in the Supporting Information of this article .

The model implementation is illustrated in the diagram of Fig. 5. The governing equations are solved with Wolfram Mathematica© 11.0 to obtain spatial distributions of temperature $T_j(z)$ and the species densities $n_{i,j}(z)$. For each set of experimental conditions ($\Phi_{CO_2}$, $p$ and $P$) the model is iterated under variation of the turbulent viscosity by means of $\nu_{\mathrm{T,peak}}$ in Eq. 9 until the simulated peak temperature $T_{\mathrm{sim}}^{\mathrm{max}}$ matches the experimental peak temperature $T_{\mathrm{gas}}$. This fitting procedure ensures that the radial turbulent transport is representative for the simulated conditions.

The simulated $\alpha_{\mathrm{sim}}$ and $\eta_{\mathrm{sim}}$ are calculated from $n_{i,j}(z = Z)$ (with $i = 1, 2, 5$ for $CO_2$, CO and C, respectively) using Eq. (1) and (2), where $Z$ is the coordinate at which temperatures $T_j$ have returned to their starting value of 300 K. For most conditions this occurs at $Z \approx 1.5$ m, with the power density profile centered on $z = 0.15$ m. At $z = Z$, both temperatures and species densities are fully mixed and uniform across all volume elements $j$, so that $n_{i,j}(z = Z)$ with any $j$ can be used to calculate $\alpha_{\mathrm{sim}}$ and $\eta_{\mathrm{sim}}$. At intermediate $z$-coordinates, where gradients exist for both temperature and species densities, it is helpful to define radially averaged values using

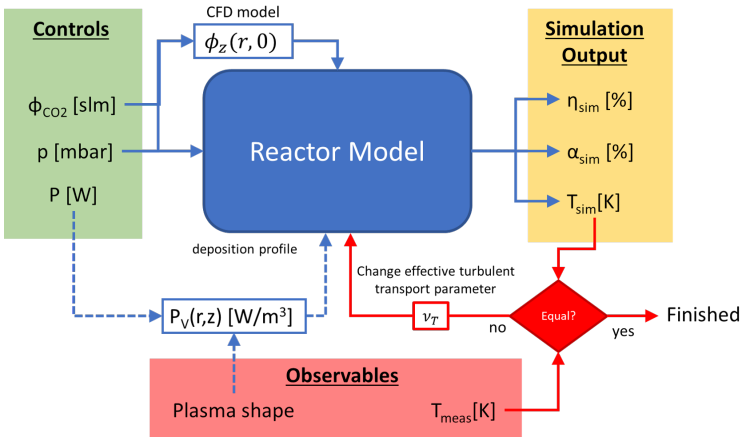


Figure 5: Diagram of the model implementation

$$\langle n_i \rangle = \frac{\sum_j v_j A_j n_{i,j}}{\sum_j v_j A_j} \quad \text{and} \tag{12}$$

$$\langle T \rangle = \frac{\sum_j n_{0,j} A_j T_j}{\sum_j n_{0,j} A_j}\,, \tag{13}$$

where the radially averaged species density at position $z$ $\langle n_i \rangle$ is determined by weighting on the species flux in a volume element and the radially averaged temperature $\langle T \rangle$ is determined by weighting on neutral density. $\langle n_i \rangle$ is used to evaluate the maximum production of CO in the reactor, as well as the loss of CO downstream from the plasma. $\langle T \rangle$ is used to determine the downstream cooling rate of the gas along the length of the reactor.

# Results and Discussion

The $CO_2$ conversion and energy efficiency are obtained for varying pressure and flow at a fixed power input of 1 kW. The energy efficiency is shown in Fig. 6 for different flow rates ranging from 2.8 to 14 slm. The corresponding simulated values of energy efficiency are shown in the adjacent panel. The error bars in the simulated values in Fig. 6 and subsequent figures indicate the propagated error from the experimental temperature data.

The particular features of the efficiency graph reveals a peak in energy efficiency in the 100-200 mbar range, which is in agreement with previous observations on $CO_2$ microwave plasmas.[5,10,36] Two pressure regimes can be distinguished. Below 110 mbar, the energy efficiency increases with pressure, while, on the other hand, the energy efficiency decreases with pressure above 110 mbar. Note also that the energy efficiency is largely independent of flow rate at low pressure, while a strong dependence occurs for high pressures. This flow

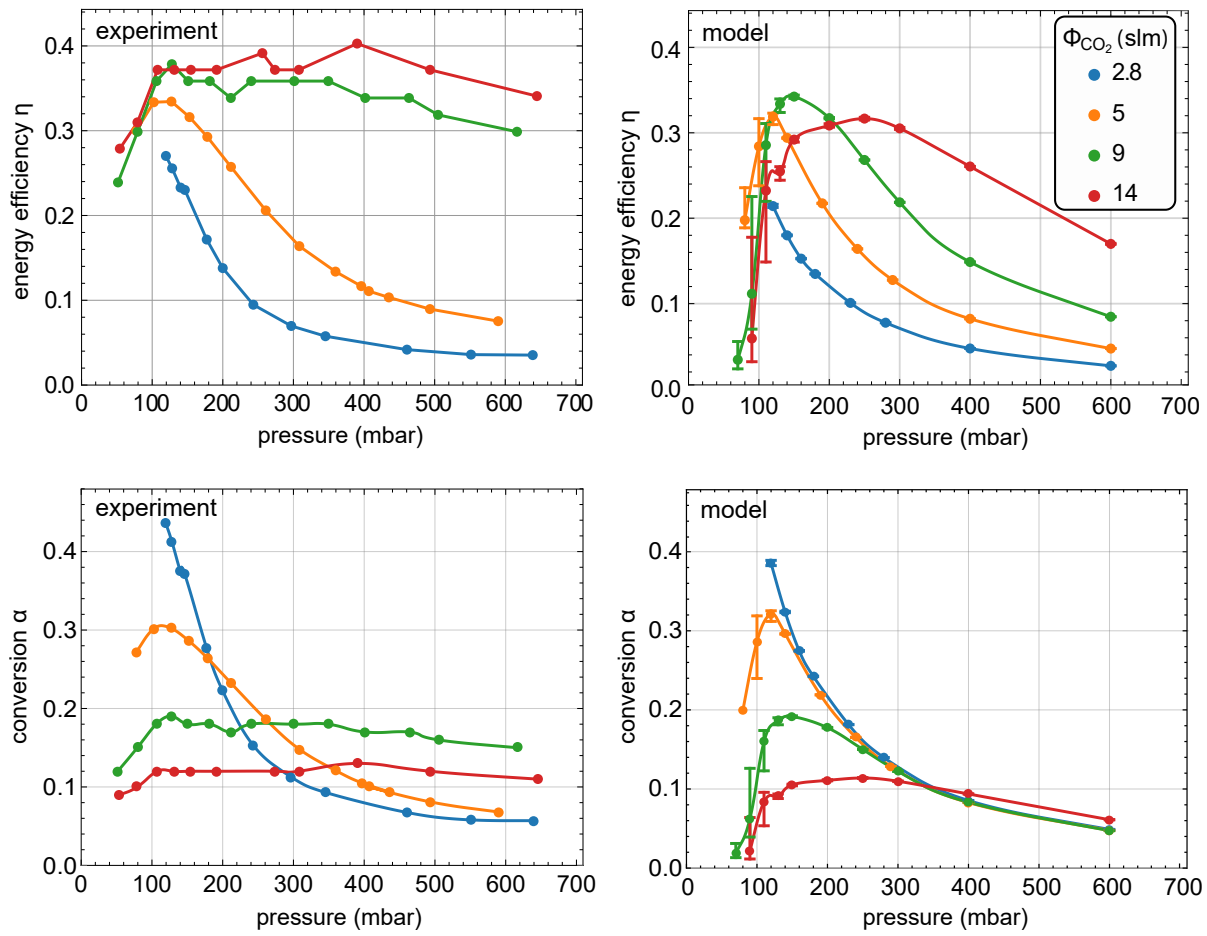


Figure 6: Energy efficiency and conversion of the dissociation process at a fixed input power of 1000 W. Left: experimental results. Right: modeling results.

dependence becomes more pronounced as pressure increases. These pressure regimes agree with the transition pressure of the L-mode and H-mode discharge conditions (cf. Fig. 1, in accordance with previously reported transition pressure around 110 mbar for a power input of 1 kW.[26] The mode transition in the 100-200 mbar regime induces a significant reduction in plasma volume (cf. Fig. 1), which results in a temperature shift from 3000-4000 K at low pressure to 5500-6500 K at high pressures.

The simulations results in Fig. 6 show a good agreement with the experimental values of $\eta$ and $\alpha$, especially considering the previously discussed simplifying assumptions made in the model with regards to the chemical kinetics and transport. The model qualitatively captures the rise in efficiency up to 110 mbar, the mode-induced peak in energy efficiency between 100 and 200 mbar, and the enhanced flow dependence at higher pressures. While good quantitative agreement is generally achieved at intermediate pressures, both conversion and energy efficiency are underestimated at the lower and higher extremes of the considered

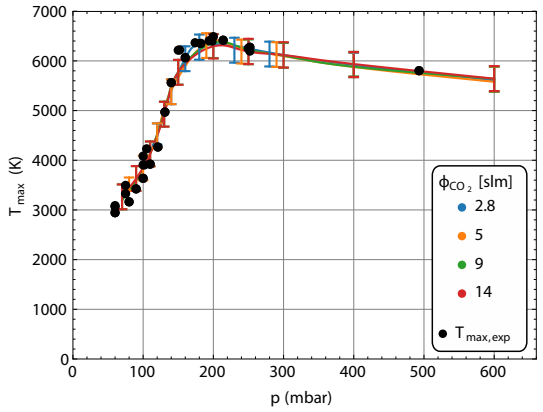


Figure 7: Experimental values of peak gas temperature in the plasma (black dots) and simulated values under conditions of matched $\nu_T$

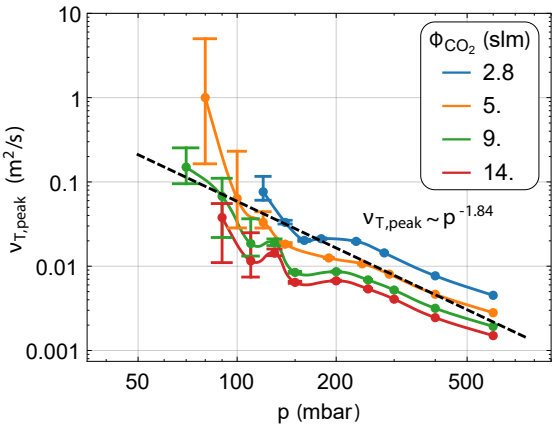


Figure 8: Fitted values of $\nu_T$ required to match simulated and experimental temperature in Fig. 7.

pressure range. We find that a match between simulated and measured temperature, as shown in Fig. 7, could only be obtained when turbulent transport has a significant contribution, in line with previous numerical CFD studies on vortex-contained gliding arc plasmas.[29] The fitted transport values in Fig. 8 reveal a $\nu_\mathrm{T} \propto p^{-1.84}$ dependency, which shows that the turbulent viscosity scales by roughly two orders of magnitude in the pressure range from 70 mbar to 500 mbar. In the lower pressure range, the contributions of the turbulent terms of $D_\mathrm{eff}$ and $\lambda_\mathrm{eff}$ exceed the laminar terms by a factor 10-100. At higher pressure, on the other hand, the turbulent and laminar terms become similar in value. This pressure dependence likely results from declining turbulent velocity fluctuations as the neutral density increases, although further analyses is required to confirm this. Despite the decline of the turbulent terms with pressure, radial diffusion still dominates over advection at elevated pressures (cf. Fig. 9) due to the sharp radial gradients in concentration and temperature associated with the H-mode plasmas. Without the inclusion of radial transport, in some H-mode plasma conditions above 200 mbar the simulated gas temperatures overestimated the measured plasma temperature by more than a factor 4 ($T_\mathrm{sim} > 20\,000$ K). The strong impact of radial transport on the particle and energy balance of the plasma in the model shows that incorporation of (turbulence-enhanced) radial transport is essential to accurately model the (plasma)-chemical processes of the vortex-stabilized $CO_2$ microwave plasma.

## Transport timescales

The strong dependency between pressure and energy efficiency is further investigated by quantifying the main CO production and loss mechanisms in and around the plasma region. For this, the timescales of energy- and heavy particle transport, as well as effects of CO

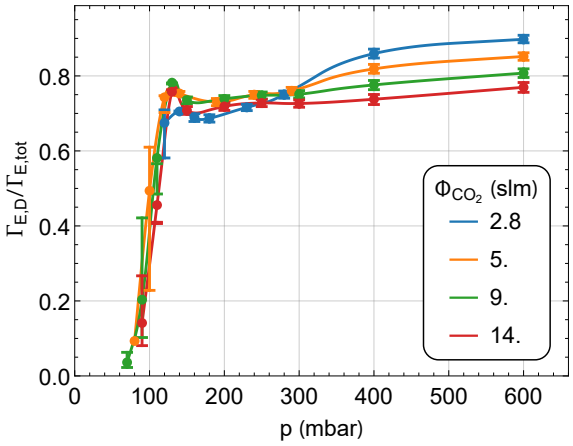


Figure 9: The fraction of net diffusive energy transport from the plasma $\Gamma_{\mathrm{E,D}}$ over the total energy flux.

recombination in the recombination trajectory are quantified in the following sections.

**Energy confinement time** Under steady state conditions the energy confinement time $\tau_E = W/P_{\mathrm{loss}}$ represents the rate of energy loss from the plasma in relation to the global energy content $W$. Under assumption of a local chemical equilibrium (ce) in the plasma, the energy confinement time of the plasma can be determined straightforwardly:

$$\tau_{\mathrm{E,ce}} = \frac{\Delta W(p,T)}{P_{\mathrm{V}}}. \tag{14}$$

Here $\Delta W(p,T)$ is the heating enthalpy per unit volume of the reactive mixture in the high-temperature phase of the thermal dissociation process with respect to pure $CO_2$ at room temperature (Eq. (18)) and $P_{\mathrm{V}}$ is local power density. The modeled value of $\tau_{\mathrm{E}} = W/(\Gamma_{\mathrm{E,A}} + \Gamma_{\mathrm{E,D}} + \Gamma_{\mathrm{E,Q}})$ consists of the confinement times of advective (A), diffusive (D), and conductive (Q) energy transport terms. The experimental values of $\tau_{\mathrm{E,ce}}$ are obtained based on the measurements of peak gas temperature and peak power density in the plasma, and are compared in Fig. 10 to the simulated values. The experimental and model-derived values of $\tau_E$ show good agreement above 100 mbar. As will become apparent, the overestimation of $\tau_{\mathrm{E,exp}}$ at low pressure arises from an implicit overestimation of the internal energy of the plasma, as the local thermal equilibrium assumption in the calculation of $\Delta W(p,T)$ breaks down at low temperature.

The fraction of diffusive energy transport in relation to the total energy transport through the plasma in Fig. 9 quantifies the relative importance of diffusive transport in the energy balance of the plasma. Here $\Gamma_{\mathrm{E,D}}/\Gamma_{\mathrm{E,tot}} = \Gamma_{\mathrm{E,D}}/(\Gamma_{\mathrm{E,A}} + \Gamma_{\mathrm{E,D}} + \Gamma_{\mathrm{E,Q}})$ is defined in Eqs. S21-S23 in the Supporting Information. Diffusive energy transport clearly dominates at high pressure, as it provides approximately 80 % of the total energy transport from the plasma

in the pressure region where the discharge contraction gives rise to the strongest radial temperature gradients. Advective transport prevails at low pressure, as the radial gradients are less pronounced due to a more uniform power deposition profile associated with the L-mode discharges in the lower pressure range.

**Particle residence time** Where the energy confinement time characterizes the timescale of energy flow through the plasma, the heavy particle confinement time is a measure of particle residence time $\tau_{\mathrm{res}}$ in the plasma. The value of $\tau_{\mathrm{res}}$ is particularly relevant in relation to the kinetic timescale of chemical conversion, $\tau_{\mathrm{eq}}$ (i.e. the timescale of chemical equilibration of the mixture), as it characterizes the extent to which chemical reactions occur within the processing time. Here we define $\tau_{\mathrm{eq}}$ as the time required to reach 95 % of the equilibrium composition in terms of CO concentration. A local chemical equilibrium in the high temperature zone may only be reasonably assumed when $\tau_{\mathrm{eq}} << \tau_{\mathrm{res}}$. In the model $\tau_{\mathrm{res}}$ $(=1/(\tau_A^{-1}+\tau_D^{-1}))$ where $\tau_{\mathrm{A}}$ and $\tau_{\mathrm{D}}$ denote the characteristic times of particle replacement in the plasma core by advective and diffusive transport, respectively.

Figure 11 shows the simulated values of $\tau_{\mathrm{res}}$ and $\tau_{\mathrm{eq}}$ in relation to the discharge pressure. It is apparent that the temperature shifts induced by the plasma mode transitions therefore results in distinct low- and high pressure flow-kinetic regimes: At low pressure ($\tau_{\mathrm{eq}} \geq \tau_{\mathrm{res}}$), while at high pressure $\tau_{\mathrm{eq}} \ll \tau_{\mathrm{res}}$. $\tau_{\mathrm{eq}}$ scales exponentially with gas temperature according to the Arrhenius behavior of the reaction rates, which explains the strong increase in the chemical reaction timescale in the low pressure range. Consequently, the conversion at low pressure is production-limited, not only due to the limited efficiency of the thermal conversion process at low temperatures, but also because of the slow chemical kinetics in relation to the transport timescales. At high pressure, $\tau_{\mathrm{res}}$ remains between 0.1-1 ms over a wide pressure and flow range. This relatively insensitivity to pressure and flow is explained by the fact that both the plasma size and temperature stabilize for fixed power input in H-mode conditions.[26]

## CO retention in the quenching trajectory

The change in CO in downstream from the high temperature region is quantified by the CO retention fraction $\gamma_{\mathrm{CO}}$

$$\gamma_{\mathrm{CO}} = \frac{\langle \Phi_{\mathrm{CO}} \rangle^{(z=Z)}}{\langle \Phi_{\mathrm{CO}} \rangle^{\mathrm{max}}} \ . \tag{15}$$

Here $\langle \Phi_{\mathrm{CO}} \rangle^{(z=Z)}$ is the stabilized CO particle flux at an axial position $Z$ far from the plasma and $\langle \Phi_{\mathrm{CO}} \rangle^{\mathrm{max}}$ is the peak value along the tube axis. As $\gamma_{\mathrm{CO}}$ is obtained from averages over the tube cross-section, it represents the net balance between production and loss of CO and provides a useful measure of the extent to which CO is retained in the cooling trajectory of dissociation products.

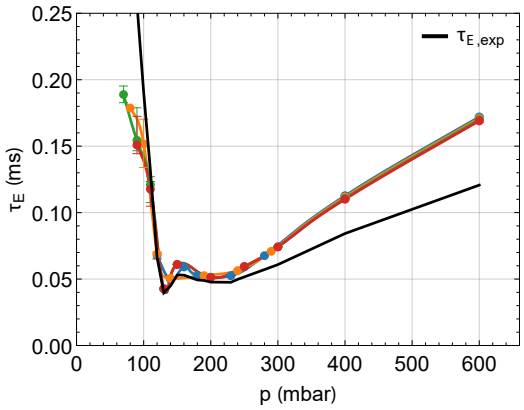


Figure 10: Simulated values of the energy confinement time $\tau_{\mathrm{E}}$ in comparison with the experimentally obtained value $\tau_{\mathrm{E,exp}}$

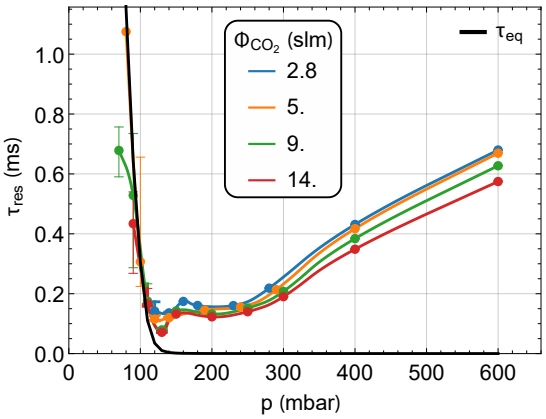


Figure 11: Simulated values of residence time $\tau_{\mathrm{res}}$ in comparison with the timescale of chemical kinetics $\tau_{\mathrm{eq}}$

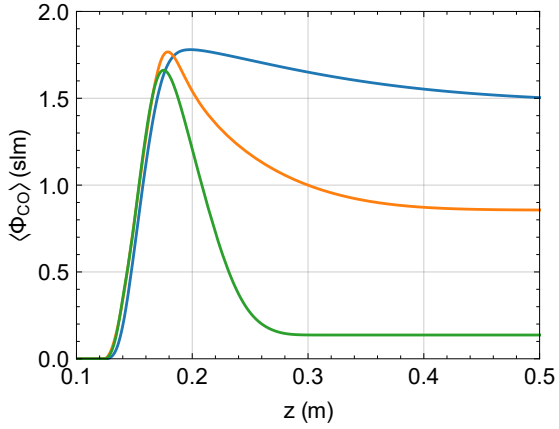


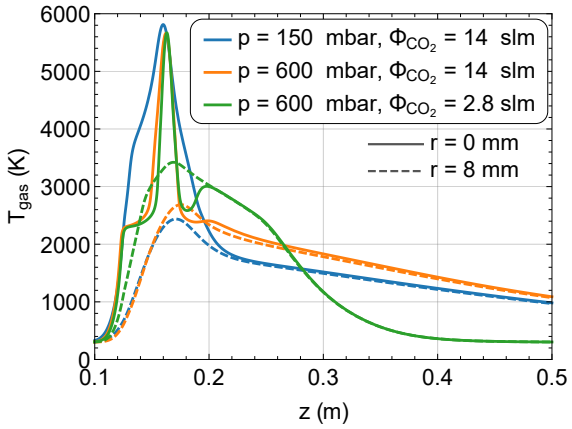


Figure 12: Simulated axial profiles of average CO flow rate along the axial coordinate $\langle\Phi_{\mathrm{CO}}\rangle$ (left) and the gas temperature at r=$0\,\mathrm{mm}$ and r=$8\,\mathrm{mm}$ (right) for different combinations of pressure and $CO_2$ flow rate.

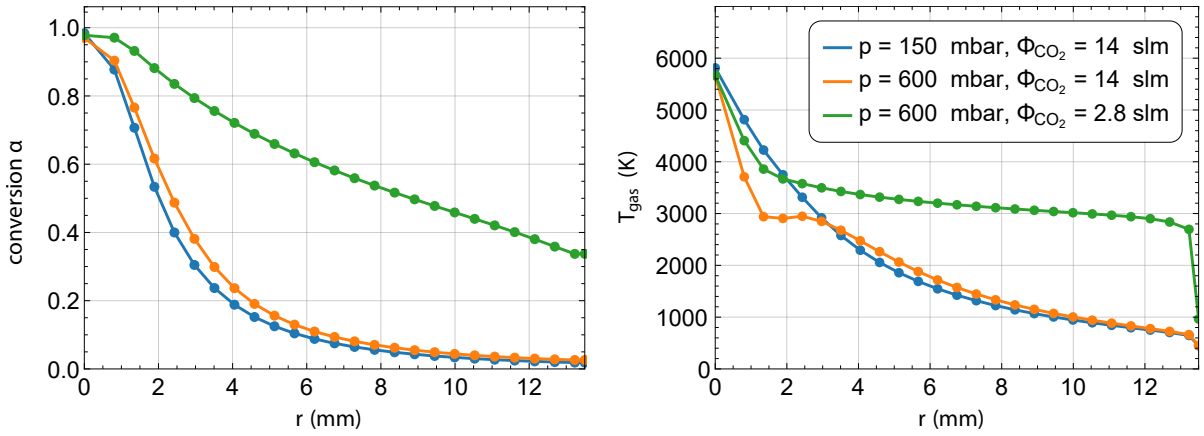


Figure 13: Simulated radial profiles of local $CO_2$ conversion $\alpha$ and gas temperature $T_{\mathrm{gas}}$ at the axial position corresponding to the peak plasma temperature (z = 0.16m), shown for high and low pressure conditions and flow rates.

Figure 12 shows typical simulated axial and radial profiles of $\langle \Phi_{\mathrm{CO}} \rangle$ and $\langle T \rangle$ for several combinations of pressure and flow. Here, the location of the heat source coincides with the profile peaks at around $z = 0.15\,\mathrm{m}$. The corresponding radial profiles at the axial position of highest temperature are shown in Fig 13. The low pressure conditions at 150 mbar and 14 slm show a modest decline in $\langle \Phi_{\mathrm{CO}} \rangle$, from at most 1.7 slm close to the heat source to 1.4 slm far downstream. Using Eq. 15 for these control parameters we find $\gamma_{\mathrm{CO}} \approx 0.80$, i.e. roughly 20 % of the CO produced in the high temperature zone is converted back to $CO_2$ in the cooling trajectory. The net loss of CO downstream from the hot zone clearly increases with pressure, indicated by the strong drop in $\langle \Phi_{\mathrm{CO}} \rangle$ in the simulations at 600 mbar in comparison to the 150 mbar conditions. Such pressure effects are expected as recombination of CO to $CO_2$ requires a third body. Even so, the recombination losses at high pressure are mitigated by enhanced flow rates: $\gamma_{\mathrm{CO}}$ increases significantly from 10 % to approximately 50 % when the flow rate is increased from 2.8 to 14 slm.

We now consider the impact of $\gamma_{\mathrm{CO}}$ on the efficiency of the overall conversion process. An overview of $\eta$ as function of the $\gamma_{\mathrm{CO}}$ is provided in Fig. 14. Two regimes, highlighted by their distinct background colors, correspond roughly to the L-mode and H-mode plasma conditions. Most CO is retained in the post-discharge of L-mode plasmas, since $\gamma_{\mathrm{CO}} > 0.8$ under these conditions. Despite the high CO retention in the post-plasma region, the overall efficiency in general remains limited under these conditions due to the unfavorable reaction timescales and thermodynamic energy efficiency previously associated with the L-mode plasmas. The higher pressure H-mode conditions, on the other hand, describe a much larger range of $\gamma_{\mathrm{CO}}$ values between 0.1 and 0.8, indicating a more substantial impact of recombination kinetics under influenced of both changes in the pressure and $CO_2$ input flow

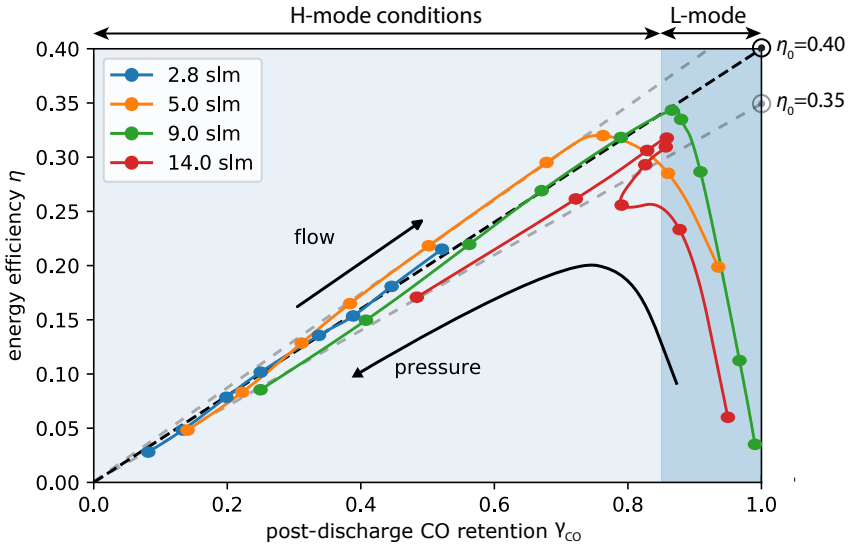


Figure 14: Modeled post-discharge CO retention $\gamma_{\mathrm{CO}}$. Indicated are the recombination limited regime of the H-mode conditions (light blue background) and the production limited regime of the L-mode discharge conditions (dark blue background).

(indicated by the arrows).

The H-mode data points in Fig. 14 are well described by

$$\eta = \eta_0 \cdot \gamma_{\mathrm{CO}}, \tag{16}$$

where $\eta_0$ represents the efficiency of the conversion process in the high temperature zone of the reactor while excluding the subsequent (downstream) kinetics of the dissociation products. The dashed lines illustrate points of equal $\eta_0$. For fixed mass flow rate $\Phi$ the value of $\eta_0$ is roughly constant with pressure under H-mode conditions, with values only varying between $0.35 < \eta_0 < 0.44$ for the entire range of mass flow rates. As $\eta$ is directly proportional to the reactor output CO flux ($\Gamma_{\mathrm{CO}}$) according to its definition in Eq. (2), Eq. (16) can be rewritten as

$$\Gamma_{\mathrm{CO}} = \Gamma_{\mathrm{CO,prod}} \cdot \gamma_{\mathrm{CO}}, \tag{17}$$

which shows that $\gamma_{\mathrm{CO}}$ relates the net source flux of CO from the high temperature region $\Gamma_{\mathrm{CO,prod}}$ to the reactor output $\Gamma_{\mathrm{CO}}$. Consequently, the behavior of Eq. (16), which describes a similar $\eta_0$ value for all H-mode conditions, shows that at a fixed power input the H-mode conditions lead to similar net production rates of CO in the high temperature region of the reactor. The changes in energy efficiency induced by pressure and flow rate, on the other hand, are attributed to changing kinetics in the cooling trajectory of the plasma products. It is important to realize that the current analysis of the simulation results, assessed using the $\Gamma_{\mathrm{CO}}$ parameter, considers averages of net production and destruction of species rather

than distinct CO production and loss routes. A more in depth analysis of the simulation results, in which the individual reaction rates in the plasma and recombination regions are considered, may provide more detail on the influence of pressure, power and flow on the dominant reaction pathways.

The conditions of high $\gamma_{CO}$ qualitatively corresponds to relatively low temperatures in the afterglow region (as shown by the change in $\langle T \rangle$ downstream from the heated zone $z$ >0.15 m in Fig. 12). The simulation shows that high flow rates keep the average temperature in the recombination trajectory below 2000 K. Under such conditions, CO recombination can be largely prevented because the rate of O+O is faster than the rate of CO+O recombination for $T$ below 2000 K. Conditions of 'overheating', downstream from the high temperature region, occur at low flow and high pressure with $T$ over 3000 K. These high temperatures coincide with a strong decrease in $\langle \Phi_{CO} \rangle$. High pressure conditions enhance the CO recombination rates around the plasma, while enhanced flow rates mitigate this effect by means of a cooling effect.

We have established thus far that cooling between plasma and peripheral flows facilitates the quenching of CO reactions in the recombination trajectory. In addition, radial transport of particles and energy between periphery and reactive zones not only enhances the cooling trajectory of the reaction products, but also enhances the resupply of $CO_2$ to the reactive zones. Following Le Chatelier's principle, enhanced concentrations of $CO_2$ in the reactive zones will shift the chemical balance to the reaction products and, as reverse reactions are mitigated, enhancing the efficiency of the conversion process. Therefore, the merits of turbulent mixing on dissociation products quenching can be attributed both to cooling and product dilution.

## Reactor performance and optimization strategies

**Limits in energy efficiency** The maximal values of energy efficiency in Fig. 6, with values of up to 35 % to 40 % are more generally observed in our experiments. An apparent efficiency plateau emerges more clearly in the extensive $\alpha - \eta$ overview plot in Fig. 15, which have been obtained from our experiments with power inputs between 400-1400 W, $CO_2$ flow rate between 3-28 slm and pressure between 80-800 mbar. The limit in efficiency is 38 % as indicated by the dashed red line. Similar peak efficiency values are reported for $CO_2$ dissociation experiments in other discharge sources. For instance, the $\eta$ of 35 % at a conversion of 11 % at 650 mbar (obtained at 1 kW input power and 14 slm and without additional measures to actively cool the exhaust flow) are similar to optimal values of $\eta$ and $\alpha$ reported for atmospheric pressure gliding arc (APGA)[15,18,37] and atmospheric pressure glow discharge (APGD)[38] experiments. The global specific energy input or SEI ($\mathcal{E}_\nu \propto P_{abs}/\Phi$) is indicated by the green dashed lines. While previous studies report optimal values of energy

efficiency at SEI values of around 1 eV/molecule for vibrationally stimulated plasma-chemical conversion of $CO_2$ under sub-sonic conditions,[9,36] this does not seem to apply for the thermal conversion process. Based on the wide range of SEI values described by points of optimal efficiency in Fig. 15 the peak values of energy efficiency for thermal $CO_2$ conversion can be considered independent of the global SEI value.

Interestingly, Fig. 15 suggests that the commonly observed trade-off between energy efficiency and conversion[5,12,39] does not universal apply. While such a trade-off may indeed occur at high pressure conditions, such as previously for the high pressure conditions in Fig. 6, peak values of both efficiency and conversion can in fact be approached simultaneously in the 100-200 mbar pressure range (top right data points in Fig. 15). These points of optimal performance were found around the L-H mode transition (for instance at SI120mbar, 4 slm, 1100 W, 43 % conversion was achieved at an efficiency of 33 %) suggesting that such conditions strike an optimal balance between the production and recombination. The simulations show that under these conditions $\gamma_{CO}$ values of up to 80-90 % are achieved, while $\eta_0$ varies between approximately 0.35 and 0.43, which indicates that the CO output of the high temperature region is largely maintained in the cooling trajectory under the most favorable conditions of pressure and flow.

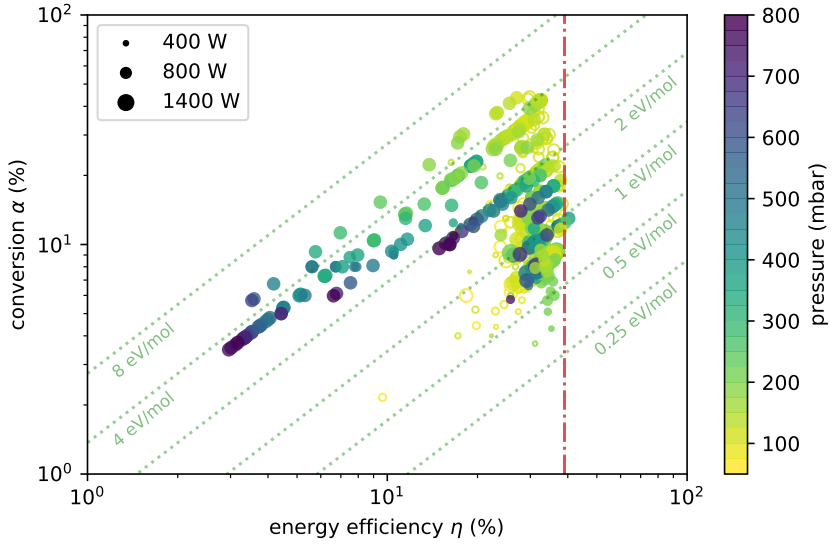


Figure 15: Overview of efficiency and conversion data in a broad range of power, flow rates and pressure. Hollow markers indicate L-mode conditions and solid markers represent H-mode plasmas.

Without the effects of turbulent mixing, product quenching relies on heat extraction from the dissociated product mixture for cooling via e.g. wall conduction or gas-dynamic expansion. This particularly holds true for high power at low flow - high global SEI conditions - where the diminished radial temperature gradients species concentrations (Fig. 13) resemble

those of homogeneous heating conditions of Fig. 2. Because of the reduced role of radial transport and mixing in such cases in the quenching process, the recombination kinetics are more true to the global kinetics models,[10,20,22] which show that cooling rates of at least $> 10^6$ K/s are required to largely prevent product recombination. In order to achieve these rates, high-SEI operation scenarios asks for measures which enhance heat extraction in the afterglow by means of e.g. active wall cooling and expansion nozzles. High conversion under high power and low flow rates have been achieved by immediate expansion of the plasma products to vacuum.[11] Moreover, super-sonic expansion nozzles may serve a more sophisticated alternative approach to facilitate the quenching of plasma products.[40] Since no specific measures were taken in our current experiment to enhance heat extraction or expansion of the dissociated products, improvements to the cooling trajectory achieved by such measures in future experiments may lead to better performance at high SEI conditions.

**Thermodynamic efficiency of thermal conversion** The narrow range of $\eta_0$ values, obtained in the simulations for a wide range of pressures and flow, are similar in value to the energy efficiency limit observed in our experiments. Figure 15 shows that an efficiency limit of just below 40 % manifests itself over a broad range of input parameters, in particular gas flow rate and power.

The limiting recombination mechanisms remain to be evaluated in the model, for instance by a more in-depth kinetic pathway analysis. Even so, it is insightful to compare the observed efficiency plateau in relation to the thermodynamic limitations in energy efficiency, based on predefined kinetic pathways of product recombination (or quenching scenarios) under closed system conditions (i.e. homogeneous conversion without transport). For this, we consider the isobaric heating of a closed volume of $CO_2$ at a pressure $p$ as function of the gas temperature $T$. In a state of chemical equilibrium, in which all possible forward and reverse chemical reaction rates are balanced ($t \to \infty$), the mole factions $x_i(p,T)$ of species $i$ are described by the minimal Gibbs free energy of the system.[41] The enthalpy change $\Delta W$ of the equilibrium gas mixture, heated from $T_0$ to an upper temperature $T_\mathrm{h}$, can be expressed as

$$\Delta W = h_\mathrm{eq}(p, T_\mathrm{h}) - h_\mathrm{eq}(p, T_0)\,. \tag{18}$$

The mixture enthalpy in chemical equilibrium $h_\mathrm{eq}(p,T)$ is calculated under assumption of ideal mixing from the total enthalpy of each individual component $h_i(T)$ and equilibrium composition

$$h_\mathrm{eq}(p,T) = \sum_i x_i(p,T) h_i(T)\ , \tag{19}$$

where $h_i$ are described by polynomials of which the coefficients are obtained from reference literature.[42]

The formation enthalpy in the heated phase $\Delta H_{\mathrm{form}}$, which characterizes the enthalpy change that leads to formation (as opposed to heating of internal and translational degrees of freedom) is obtained by considering the change in composition without heating in the mixture enthalpy $h_{\mathrm{eq,form}} = \sum_i x_i(p, T_h) h_i(T_0)$ (note the $T_0$ in the enthalpy factor with respect to Eq. (19))

$$\Delta H_{\mathrm{form}} = h_{\mathrm{eq,form}}(p, T_{\mathrm{h}}) - h_{\mathrm{eq}}(p, T_0) \tag{20}$$

The thermal formation fraction, defined by the ratio of formation enthalpy to total enthalpy change,

$$\frac{\Delta H_{\mathrm{form}}}{\Delta W} = \frac{\sum_i \left[x_i(p, T_{\mathrm{h}}) h_i(T_0) - x_i(p, T_0) h_i(T_0)\right]}{\sum_i \left[x_i(p, T_{\mathrm{h}}) h_i(T_{\mathrm{h}}) - x_i(p, T_0) h_i(T_0)\right]} \tag{21}$$

represents the faction of energy invested in chemical decomposition (indicated as the blue line in Fig. 16.

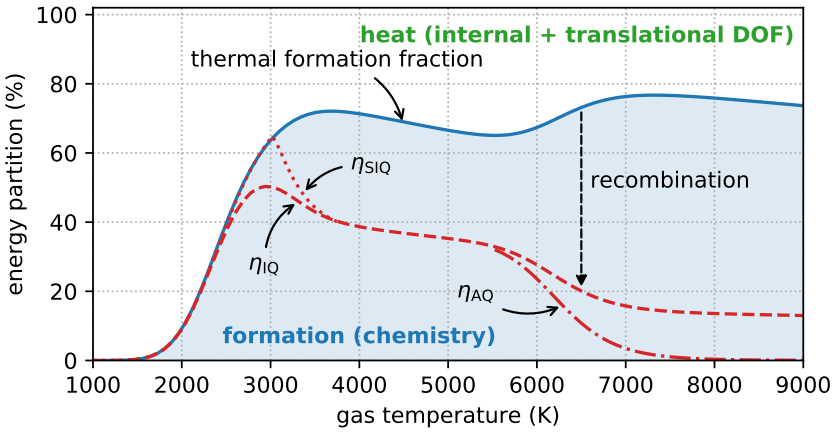


Figure 16: The partition of energy into heat and formation for various thermal conversion scenarios calculated for pressure of 100 mbar and starting at chemical equilibrium composition at temperature $T$. The net efficiencies $\eta$ of the thermal dissociation process via absolute (AQ), ideal (IQ) and super-ideal (SIQ) quenching scenarios are indicated in red.

In Fig. 16 the thermodynamic efficiency limit is calculated under three distinct recombination trajectories: absolute quenching conditions ($\eta_{\mathrm{AQ}}$), in which CO production in the high temperature phase is retained; ideal quenching conditions ($\eta_{\mathrm{IQ}}$), in which the $CO_2$ conversion achieved in the high temperature phase is conserved; and a super-ideal quenching scenario ($\eta_{\mathrm{SIQ}}$), in which all atomic oxygen is assumed to react with a $CO_2$ molecule under formation of an additional CO. Under ideal quenching conditions where all atomic oxygen fully associates to $O_2$ rather than recombination with CO to $CO_2$, the energy efficiency is $\eta_{\mathrm{IQ}} =$ 30-50 % for a temperature of 3000-6000K in the high temperature region. Furthermore, the calculations predict values of around $\eta_{\mathrm{IQ}} = 50\,\%$ when the dissociation process takes place

at around 3000 K. However, as previously established, the residence times in this regime are insufficient to accommodate the relatively slow chemical kinetics timescales. Therefore, the increase of particle residence times in future experiments is a viable approach for increasing the energy efficiency at low pressure, e.g. by adjustment of the plasma size, flow geometry or the vortex intensity. While thermodynamic limits imposed by ideal quenching is a plausible explanation for the observed maxima in $\eta$, it is important to realize that the further analysis of the individual reaction rates is required to provide more solid insight in to the distinct reaction pathways.

The peak in $\eta_{\mathrm{SIQ}}$, a notable feature which occurs at a temperature of 3000 K, coincides with the depletion of $CO_2$ in the high temperature phase. Consequently, with further increase of temperature $\eta_{\mathrm{SIQ}} = \eta_{\mathrm{IQ}}$ is approached. Moreover, the deviation of $\eta_{\mathrm{IQ}}$ and $\eta_{\mathrm{AQ}}$ at temperatures above roughly 6000 K is associated with the production of atomic carbon. Note that the limiting effect of $CO_2$ depletion in preceding closed-system calculations is lifted when considering the admixture of additional $CO_2$ in open system situation in which particle transport may occur. This suggests that the evident efficiency gains of a super-ideal quenching trajectory can be extended to higher temperatures.

In the further assessment of the quenching mechanisms, the $CO_2 + O \rightarrow CO + O_2$ reaction deserves particular attention. Stimulation of this reaction in the cooling trajectory increases the energy efficiency in comparison to ideal quenching since the energy contained in reactive oxygen is used more efficiently; to produce an additional CO molecule as apposed to heat production following alternative recombining reactions with O or CO. The thermodynamics of a super-ideal quenching scenario indicate that an upper efficiency of approximately 70 % are feasible, but only in an open system in which sufficient $CO_2$ is supplied to react with all plasma-produced atomic oxygen. It is interesting to note that the thermal dissociation process under optimized super-ideal quenching conditions comes close to the efficiency values of 80 % previously reported under supposed conditions of vibrational non-equilibrium,[8] suggesting that the latter may be explained also with a dominant contribution of thermal chemistry.

The vibrational dissociation process relies on a super-ideal quenching of reaction products for high efficiencies just like the thermal conversion process, as demonstrated in kinetic simulations of the non-equilibrium process.[32] However, the practical feasibility of the super-ideal quenching pathway remains unclear. The activation barrier of 1.57 eV inhibits the $CO_2 + O$ reaction pathway.[32] While conditions of high VT-non-equilibrium have been previously associated with vibrational activation of the $CO_2 + O$ reaction,[36] the merits of reactant pre-excitation (i.e. vibrationally, electronically) remains to be verified experimentally. Also, feasible methods for leveraging this pre-excitation to enhance super-ideal quenching conditions in thermal regime must be established. This motivates the further investigations of the

$CO_2 + O$ reaction in future iterations of the model.

**Improvement of model accuracy** While the good qualitative agreement between experiment and model in the preceding analysis has provided valuable insight into the mechanisms of CO production and destruction, the predictive capability and accuracy of the model may still be improved. This holds in particular for the quantitative deviations that occur at high and low pressure. We can already speculate on plausible causes based on the present analysis of the simulation results.

The underestimation of $\alpha$ and $\eta$ at high pressure and flow rate suggest that both $\eta_0$ and $\gamma_{CO}$ are underestimated in the model. It therefore appears that both the rate of CO production in the high temperature region of the reactor and the recombination rates in the quenching region are underestimated. Deviations likely stem from the flow implementation and possible inaccuracies introduced with the chemical mechanism. The simplified representation of the flow geometry, composed out of advective transport only in axial direction and diffusive transport only in radial direction, likely over-simplifies spatial features of the complex vortex flow dynamics such as the convective recirculation cell. With potential implications for both the particle residence times and quenching trajectory, over-simplification of the flow geometry may explain the deviations at low pressure, where the state of chemical non-equilibrium is sensitive to deviations in particle transport, but also at high pressures, where turbulent mixing plays an important role in the recombination process. Therefore, steps taken to more closely integrate CFD simulations and reaction kinetics may improve the general accuracy of the reactor model. Such attempts do, however, rely critically on CFD models which accurately describe flow patterns and turbulent transport in locally heated swirling flows. Lastly, the accuracy of the employed $CO_2$ chemical mechanism remains a point of concern, as presently thermodynamic consistency is ensured (i.e. development towards the correct equilibrium composition) while the characteristic timescales remain to be validated.

**Challenges of non-uniform discharge characterization** Despite a frequent use in the context of plasma-chemical conversion, the global specific energy input does not accurately describe localized conditions of non-uniform discharges. In the microwave plasma we find that power input $P_{abs}$ mostly influences production in the plasma while flow rate $\Phi$ influence mostly recombination kinetics, showing that the global SEI $\propto P_{abs}/\Phi$ uniquely characterizes neither the plasma state nor the overall reactor performance. Such differences in response to changes in power and flow for values of global SEI have been previously reported also for other discharges with a non-uniform nature such as DBDs.[43] Therefore, the practice of using SEI as a universal plasma state variable as basis of comparison between individual

non-uniform plasma flow reactor experiments cannot be justified and should, therefore, be avoided. To alleviate the limitations of the global SEI parameter, Van den Bekerom et al.[34] has proposed the local SEI parameter which accounts for the dimensions of the heated region. However, as shown by the particle residence time and energy confinement time analysis in this work, the particle flows in turbulent plasma environments (and by extension the local SEI values) rely strongly on the advective and diffusive transport. Consequently, studies of non-uniform plasma reactors which utilize the SEI parameter (global or local) without considering these factors are susceptible to large error.

The distinct discharge modes and its changes with pressure profoundly influence reactor performance. We have shown that the peak in efficiency around 100 - 200 mbar coincides with a plasma mode transition and is related to shifts occurring in the production (stimulated by plasma temperature) and destruction (pressure-induced 3-body recombination and flow parameters) rates. This finding explains the moderate pressure microwave plasma performance dynamics based solely on thermally driven chemistry effects, and thereby provides a alternative to previously accepted theories[5,23,36] in attribute such effects to the changes to the extent of VT-nonequilibrium in the plasma. In addition to the strong dependence on pressure, parameters such power input[25] and gas composition[44] may also significantly influence the contracted state of the plasma and, consequently, the plasma chemistry. For instance, studies of trace gas admixture may induce changes in the charged particle kinetics not only due to changes in composition, but also due to the changes in local power density due to contraction. As such effects are not easily distinguished, the possible changes in plasma uniformity subject to changes in the process parameters of interest should always be carefully considered. This shows that a thorough understanding of plasma contraction phenomena and non-uniformity are key in the correct interpretation of the performance of plasma-chemical conversion experiments.

# Concluding remarks

The present study investigates the implications of non-uniform heating on the dissociation and recombination mechanisms in the vortex-stabilized $CO_2$ microwave discharge. For this, a newly developed 2D axisymmetric tubular reactor model is presented which captures the essential aspects of plasma kinetics and transport validated with experimentally obtained values of temperature and power density distribution. The model is used to disentangle the mechanisms of CO production and recombination.

A 2D axisymmetric tubular chemical kinetics model is developed, aiming to combine the elements of discharge contraction, turbulent transport, and thermal chemistry. The model reproduces the strong pressure dependence of energy efficiency of the plasma-conversion

process in the 80 - 600 mbar range with good qualitative agreement for flow rates between 2.8 - 14 slm. Both the experiments and model reach energy efficiency values up to approximately 40 % under favorable combinations of flow and pressure. The model results suggest that the CO flux originating from the high temperature region is only reduced by roughly 10-20 % during cooling in the afterglow of the plasma. Pressure-induced recombination effects can be quite significant, however, with the simulations indicating up to 90 % loss of CO in the cooling trajectory at high pressure and low flow rate. There is an eminent role for radial transport in facilitating the quenching process by providing both cooling and dilution through diffusive mixing. The radial admixture of $CO_2$ can largely mitigate the pressure-enhanced recombination effects up to atmospheric pressure, but this comes at the cost of low conversion.

The simulation results show that the discharge modes of the $CO_2$ microwave plasma induce distinct quasi-thermal chemical-kinetic regimes. Low pressure L-mode conditions limit the CO production in the plasma due to slow dissociation rates, related to relatively low plasma temperatures. High pressure H-mode plasma conditions, on the other hand, are associated with energy efficiency limitations resulting from downstream recombination processes. The transition conditions between 100 - 200 mbar provide a favorable trade-off between the dissociation rates in the plasma (which increase with pressure as a result of contraction-induced temperature rise with pressure) and pressure-stimulated recombination effects, and explains the more common observation of favorable $CO_2$ microwave reactor conditions in this particular pressure regime.

Both an accurate depiction of power density distribution under influence of contraction phenomena, as well as the turbulent transport in and around the plasma, are vital for the predictive capabilities of the model. The conversion and recombination processes in the high temperature zone and cooling trajectory should be further evaluated to establish the dominant reaction pathways and their limitations on the overall conversion process. For this, present quantitative deviations between experiment and model, which occur in at low and high pressure in particular, must be addressed. The accuracy of the present model may by improved by refinements of the simplified vortex flow implementation. Furthermore, the reliability of the kinetics scheme under the present high-temperature conditions must be evaluated. In general, research devoted to the development of accurate models for discharge contraction dynamics in molecular plasmas represent a fruitful ground for improving the predictive capabilities of non-uniform plasma reactor models.

Further prospects for efficiency enhancement in the thermal $CO_2$ plasma remain. The important role of kinetics and turbulent transport in the cooling trajectory shows that optimization of the post-discharge environment, rather than the plasma environment, offers most opportunities for improvement of the plasma-chemical conversion process.

## Acknowledgment

This research has been carried out as part of the Plasma Power to Gas research program with reference 13581, which is co- financed by the Netherlands Organization for Scientific Research (NWO) and Alliander N.V. The authors would like to acknowledge Guy Frissen and Tim Righart for their valuable contributions related to the conversion and temperature measurements, respectively.

## Supporting Information Available

Data underlying this article can be accessed on Zenodo at DOI: **10.5281/zenodo.3909487** and used under the Creative Commons Attribution 4.0 license.

## References

(1) Conrads, H.; Schmidt, M. Plasma generation and plasma sources. *Plasma Sources Sci. Technol.* **2000**, *9*, 441–454.

(2) Lebedev, Y. A. Microwave discharges at low pressures and peculiarities of the processes in strongly non-uniform plasma. *Plasma Sources Sci. Technol.* **2015**, *24*, 053001.

(3) Brandenburg, R.; Bogaerts, A.; Bongers, W. A.; Fridman, A. A.; Fridman, G.; Locke, B. R.; Miller, V.; Reuter, S.; Schiorlin, M.; Verreycken, T. et al. White paper on the future of plasma science in environment, for gas conversion and agriculture. *Plasma Process. Polym.* **2019**, *16*, 1700238.

(4) Rusanov, V. D.; Fridman, A. A.; Sholin, G. V. The physics of a chemically active plasma with nonequilibrium vibrational excitation of molecules. *Uspekhi Fiz. Nauk* **1981**, *134*, 185.

(5) Snoeckx, R.; Bogaerts, A. Plasma technology-a novel solution for $CO_2$ conversion? *Chem. Soc. Rev.* **2017**, *46*, 5805–5863.

(6) Van Rooij, G. J.; Akse, H. N.; Bongers, W. A.; van de Sanden, M. C. M. Plasma for electrification of chemical industry: A case study on $CO_2$ reduction. *Plasma Phys. Control. Fusion* **2018**, *60*, 014019.

(7) Bogaerts, A.; Neyts, E. C. Plasma Technology: An Emerging Technology for Energy Storage. *ACS Energy Lett.* **2018**, *3*, 1013–1027.

(8) Legasov, V. A.; Zhivotov, V. K.; Krasheninnikov, E. G.; Krotov, M. F.; Patrushev, L.; Rusanov, V. D.; Rykunov, G. V.; Spektor, A. M.; Fridman, A. A.; Sholin, G. V. A nonequilibrium plasma-chemical process of $CO_2$ dissociation in high-frequency and ultra-high-frequency discharges. *Sov. Phys. Dokl.* **1978**, *23*, 44–46.

(9) Butylkin, Y. P.; Zhivotov, V. K.; Krasheninnikov, E. G.; Krotov, M. F.; Rusanov, V. D.; Tarasov, Y. P.; Fridman, A. A. Dissociation of $CO_2$ by a plasma-chemical process in a nonequilibrium microwave discharge. *Sov. Phys. Tech. Phys.* **1981**, *26*, 555.

(10) den Harder, N.; van den Bekerom, D. C. M.; Al, R. S.; Graswinckel, M. F.; Palomares, J. M.; Peeters, F. J. J.; Ponduri, S.; Minea, T.; Bongers, W. A.; van de Sanden, M. C. M. et al. Homogeneous $CO_2$ conversion by microwave plasma: Wave propagation and diagnostics. *Plasma Process. Polym.* **2017**, *14*, 1600120.

(11) Bongers, W. A.; Bouwmeester, H.; Wolf, A. J.; Peeters, F. J. J.; Welzel, S.; van den Bekerom, D. C. M.; den Harder, N.; Goede, A.; Graswinckel, M.; Groen, P. W. et al. Plasma-driven dissociation of $CO_2$ for fuel synthesis. *Plasma Process. Polym.* **2016**, *14*, 1600126.

(12) Britun, N.; Silva, T.; Chen, G.; Godfroid, T.; van der Mullen, J. J. A. M.; Snyders, R. Plasma-assisted $CO_2$ conversion: Optimizing performance via microwave power modulation. *J. Phys. D. Appl. Phys.* **2018**, *51*.

(13) Liu, J. L.; Park, H. W.; Chung, W. J.; Park, D. W. High-Efficient Conversion of $CO_2$ in AC-Pulsed Tornado Gliding Arc Plasma. *Plasma Chem. Plasma Process.* **2016**, *36*, 437–449.

(14) Silva, T.; Britun, N.; Godfroid, T.; Snyders, R. Understanding $CO_2$ decomposition in microwave plasma by means of optical diagnostics. *Plasma Process. Polym.* **2017**, *14*, 1600103.

(15) Ramakers, M.; Trenchev, G.; Heijkers, S.; Wang, W.; Bogaerts, A. Gliding Arc Plasmatron: Providing an Alternative Method for Carbon Dioxide Conversion. *ChemSusChem* **2017**, *10*, 2642–2652.

(16) van den Bekerom, D. C. M.; van de Steeg, A.; van de Sanden, M. C. M.; van Rooij, G. J. Mode resolved heating dynamics in pulsed microwave $CO_2$ plasma from laser Raman scattering. *J. Phys. D. Appl. Phys.* **2020**, *53*, 054002.

(17) Kotov, V.; Koelman, P. M. J. Plug flow reactor model of the plasma chemical conversion of $CO_2$. *Plasma Sources Sci. Technol.* **2019**, *28*, 095002.

(18) Wang, W.; Mei, D.; Tu, X.; Bogaerts, A. Gliding arc plasma for $CO_2$ conversion: Better insights by a combined experimental and modelling approach. *Chem. Eng. J.* **2017**, *330*, 11–25.

(19) Sun, S. R.; Wang, H. X.; Mei, D. H.; Tu, X.; Bogaerts, A. $CO_2$ conversion in a gliding arc plasma: Performance improvement based on chemical reaction modeling. *J. CO2 Util.* **2017**, *17*, 220–234.

(20) Yang, T.; Shen, J.; Ran, T.; Li, J.; Chen, P.; Yin, Y. Understanding $CO_2$ decomposition by thermal plasma with supersonic expansion quench. *Plasma Sci. Technol.* **2018**, *20*.

(21) Vermeiren, V.; Bogaerts, A. Plasma-Based $CO_2$ conversion: To quench or not to quench. *Submitt. to JPCC*

(22) Butylkin, Y. P.; Grikenko, A. A.; Levitskii, A. A.; Polak, L. S.; Rytova, N. M.; Slovetskii, D. I. Mathematical modeling of the kinetics of the thermal decomposition of carbon dioxide in an electric arc discharge and quenching of the products. *Khimiya Vysikikh Energii* **1979**, *13*, 545–551.

(23) Fridman, A. A.; Kennedy, L. A. *Plasma Physics and Engineering*; Taylor & Francis: New York, 2004.

(24) Berthelot, A.; Bogaerts, A. Pinpointing energy losses in $CO_2$ plasmas – Effect on $CO_2$ conversion. *J. CO2 Util.* **2018**, *24*, 479–499.

(25) Wolf, A. J.; Righart, T. W. H.; Peeters, F. J. J.; Groen, P. W. C.; van de Sanden, M. C. M.; Bongers, W. A. Characterization of $CO_2$ microwave plasma based on the phenomenon of skin-depth-limited contraction. *Plasma Sources Sci. Technol.* **2019**, *28*, 115022.

(26) Wolf, A. J.; Righart, T. W. H.; Peeters, F. J. J.; Bongers, W. A.; van de Sanden, M. C. M. Implications of thermo-chemical instability on the contracted modes in CO 2 microwave plasmas. *Plasma Sources Sci. Technol.* **2020**, *29*, 025005.

(27) Gutsol, A. F.; Bakken, J. A. A new vortex method of plasma insulation and explanation of the Ranque effect. *J. Phys. D. Appl. Phys.* **1998**, *31*, 704–11.

(28) Belov, I.; Vermeiren, V.; Paulussen, S.; Bogaerts, A. Carbon dioxide dissociation in a microwave plasma reactor operating in a wide pressure range and different gas inlet configurations. *J. CO2 Util.* **2018**, *24*, 386–397.

(29) Trenchev, G.; Kolev, S.; Wang, W.; Ramakers, M.; Bogaerts, A. $CO_2$ Conversion in a Gliding Arc Plasmatron: Multidimensional Modeling for Improved Efficiency. *J. Phys. Chem. C* **2017**, *121*, 24470–24479.

(30) Chang, F.; Dhir, V. Mechanisms of heat transfer enhancement and slow decay of swirl in tubes using tangential injection. *Int. J. Heat Fluid Flow* **1995**, *16*, 78–87.

(31) Bogaerts, A.; Berthelot, A.; Heijkers, S.; Kolev, S.; Snoeckx, R.; Sun, S.; Trenchev, G.; Van Laer, K.; Wang, W. $CO_2$ conversion by plasma technology: insights from modeling the plasma chemistry and plasma reactor design. *Plasma Sources Sci. Technol.* **2017**, *26*, 063001.

(32) Berthelot, A.; Bogaerts, A. Modeling of $CO_2$ Splitting in a Microwave Plasma: How to Improve the Conversion and Energy Efficiency. *J. Phys. Chem. C* **2017**, *121*, 8236–8251.

(33) Sun, H.; Lee, J.; Do, H.; Im, S. K.; Soo Bak, M. Experimental and numerical studies on carbon dioxide decomposition in atmospheric electrodeless microwave plasmas. *J. Appl. Phys.* **2017**, *122*, 1–11.

(34) van den Bekerom, D. C. M.; Palomares Linares, J. M.; Verreycken, T.; van Veldhuizen, E. M.; Nijdam, S.; Berden, G.; Bongers, W. A.; van de Sanden, M. C. M.; van Rooij, G. J. The importance of thermal dissociation in $CO_2$ microwave discharges investigated by power pulsing and rotational Raman scattering. *Plasma Sources Sci. Technol.* **2019**, *28*, 055015.

(35) Beuthe, T. G.; Chang, J. S. Chemical Kinetic Modelling of Non-Equilibrium Ar-$CO_2$ Thermal Plasmas. *Jpn. J. Appl. Phys.* **1997**, *36*, 4997–5002.

(36) Fridman, A. A. *Plasmas Chemistry*; Cambridge University Press, 2008.

(37) Nunnally, T.; Gutsol, K.; Rabinovich, A.; Fridman, A. A.; Gutsol, A. F.; Kemoun, A. Dissociation of $CO_2$ in a low current gliding arc plasmatron. *J. Phys. D. Appl. Phys.* **2011**, *44*, 274009.

(38) Trenchev, G.; Nikiforov, A.; Wang, W.; Kolev, S.; Bogaerts, A. Atmospheric pressure glow discharge for $CO_2$ conversion: Model-based exploration of the optimum reactor configuration. *Chem. Eng. J.* **2019**, *362*, 830–841.

(39) Spencer, L. F.; Gallimore, A. D. Efficiency of $CO_2$ dissociation in a radio-frequency discharge. *Plasma Chem. Plasma Process.* **2011**, *31*, 79–89.

(40) Vermeiren, V.; Bogaerts, A. Supersonic Microwave Plasma: Potential and Limitations for Energy-Efficient $CO_2$ Conversion. *J. Phys. Chem. C* **2018**, *122*, 25869–25881.

(41) Lieberman, M. A.; Lichtenberg, A. J. *Princ. Plasma Discharges Mater. Process. Second Ed.*; John Wiley & Sons, Inc.: Hoboken, NJ, USA, 2005; pp 1–757.

(42) McBride, B. J.; Zehe, M. J.; Gordon, S. *NASA Glenn coeefficients for calculating thermodynamic properties of individual species*; 2002; p 287.

(43) Aerts, R.; Somers, W.; Bogaerts, A. Carbon Dioxide Splitting in a Dielectric Barrier Discharge Plasma: A Combined Experimental and Computational Study. *ChemSusChem* **2015**, *8*, 702–716.

(44) Moisan, M.; Pelletier, J. *Physics of Collisional Plasmas*; Springer: Dordrecht, 2012.

# $CO_2$ Conversion in Non-Uniform Discharges: Disentangling Dissociation and Recombination Mechanisms

Supporting Information for publication

## Model Reactions

**Table S1: Rate constants and activation energies of the elementary reactions considered in the kinetics calculations, adapted from Butylkin et al.[22] (A) and Beuthe et al.[35] (B). The rate constant is expressed in $\mathrm{m^3 s^{-1}}$ for binary reactions and $\mathrm{m^6 s^{-1}}$ for ternary reactions.**

| No. | Reaction | $k_0$ | $E_a$ (K) | source |
|---|---|---|---|---|
| N1 | $2CO_2 \longrightarrow CO + CO_2 + O$ | $4.38 \times 10^{-13}$ | 64697 | A |
| N2 | $CO + CO_2 \longrightarrow 2CO + O$ | $4.38 \times 10^{-13}$ | 64697 | A |
| N3 | $CO_2 + O_2 \longrightarrow CO + O + O_2$ | $3.72 \times 10^{-16}$ | 60199.2 | A |
| N4 | $CO_2 + O \longrightarrow CO + O_2$ | $7.77 \times 10^{-18}$ | 18166.2 | A |
| N5 | $2O_2 \longrightarrow 2O + O_2$ | $8.14 \times 10^{-15}$ | 59684.4 | A |
| N6 | $O + O_2 \longrightarrow 3O$ | $1.99 \times 10^{-14}$ | 57820 | A |
| N7 | $CO + O_2 \longrightarrow CO + 2O$ | $2.41 \times 10^{-15}$ | 59379.9 | A |
| N8 | $CO_2 + O_2 \longrightarrow CO_2 + 2O$ | $2.57 \times 10^{-15}$ | 59626.5 | A |
| N9 | $CO + CO_2 \longrightarrow C + CO_2 + O$ | $1.46/T^{3.52}$ | 128700 | B |
| N10 | $2CO \longrightarrow C + CO + O$ | $1.46/T^{3.52}$ | 128700 | B |
| N11 | $CO + O_2 \longrightarrow C + O + O_2$ | $1.46/T^{3.52}$ | 128700 | B |
| N12 | $CO + O \longrightarrow C + 2O$ | $1.46/T^{3.52}$ | 128700 | B |
| N13 | $2CO \longrightarrow C + CO_2$ | $9.02 \times 10^{-22}$ | 70944.4 | B |
| N14 | $CO + CO_2 + O \longrightarrow 2CO_2$ | $6.54 \times 10^{-45}$ | 2183.97 | A |
| N15 | $2CO + O \longrightarrow CO + CO_2$ | $6.54 \times 10^{-45}$ | 2183.97 | A |
| N16 | $CO + O + O_2 \longrightarrow CO_2 + O_2$ | $6.51 \times 10^{-48}$ | -1856.72 | A |
| N17 | $CO + O_2 \longrightarrow CO_2 + O$ | $1.23 \times 10^{-18}$ | 15359.7 | A |
| N18 | $2O + O_2 \longrightarrow 2O2$ | $6.81 \times 10^{-46}$ | 0 | A |
| N19 | $3O \longrightarrow O + O_2$ | $2.19 \times 10^{-45}$ | -2340.47 | A |
| N20 | $CO + 2O \longrightarrow CO + O_2$ | $2.76 \times 10^{-46}$ | 0 | A |
| N21 | $CO_2 + 2O \longrightarrow CO_2 + O_2$ | $2.76 \times 10^{-46}$ | 0 | A |
| N22 | $C + CO_2 + O \longrightarrow CO + CO_2$ | $9.1 \times 10^{-34}/T^{3.08}$ | -2114 | B |
| N23 | $C + CO + O \longrightarrow 2CO$ | $9.1 \times 10^{-34}/T^{3.08}$ | -2114 | B |
| N24 | $C + O + O_2 \longrightarrow CO + O_2$ | $9.1 \times 10^{-34}/T^{3.08}$ | -2114 | B |
| N25 | $C + 2O \longrightarrow CO + O$ | $9.1 \times 10^{-34}/T^{3.08}$ | -2114 | B |
| N26 | $C + CO_2 \longrightarrow 2CO$ | $9.02 \times 10^{-22}$ | 0 | B |

# Model Equations

**Continuity equations** A system of coupled mass and energy balances are solved for each volume element $j$ at axial coordinate $z$ to obtain radial and axial temperature and species distributions. For computational efficiency, the number of volume elements in the radial direction was limited to J = 25. It is implicitly assumed that within a single volume element $j$ the fluid is perfectly mixed in the radial directions, both in terms of species densities $n_j^i$ and axial velocity component $v_j$. The mass balance for species $i$ and volume element $j$ is given by

$$\frac{\partial v_j(z) n_j^i(z)}{\partial z} = R_j^i\left(z\right) - \Lambda_j^i\left(T_{j-1}(z), T_j(z), T_{j+1}(z), z\right), \tag{S1}$$

and the energy balance for each volume element $j$ by

$$\frac{\partial}{\partial z}\left(\sum_i v_j(z)\cdot n_j^i(z)\cdot H^i\left(T_j(z)\right)\right) = \left(\sum_i H^i\left(T_j(z)\right)\cdot \Lambda_j^i\left(T_{j-1}(z), T_j(z), T_{j+1}(z), z\right)\right) + Q_j\left(T_{j-1}(z), T_j(z), z\right)\ , \tag{S2}$$

where $R_j^i(z)$ [$\mathrm{m^{-3}s^{-1}}$] is the chemical source term, $\Lambda_j^i$ [$\mathrm{m^{-3}s^{-1}}$] the net loss or gain of species $i$ from volume element $j$ through radial transport, $H^i$ [J] the enthalpy per particle of species $i$ and $Q_j$ [$\mathrm{Jm^{-3}s^{-1}}$] the net heat flux from volume element $j$. The cross-sectional area of a volume element $A_j$ [$\mathrm{m^2}$] is calculated from the radial position of volume element boundaries $r_j$ using

$$A_j = \pi\left(r_j^2 - r_{j-1}^2\right). \tag{S3}$$

The ideal gas law provides an additional equation of state by imposing a constant pressure $p$ throughout the reactor volume:

$$p = k_b T_j(z) n_{0,j}(p, T_j(z)) = const\ , \tag{S4}$$

where $n_{0,j}(p, T_j(z)) = \sum_i n_j^i(z)$ is the number density of neutral species.

Following these equations, the velocity in each volume element is described by

$$v_j[z] = \frac{\dot{m}}{A_j \overline{M}_j(z) n_{0,j}(p, T_j(z))}\ , \tag{S5}$$

Here, $\dot{m}$ is the total mass flow into the system and $\overline{M}_j(z)$ is the mean molar mass which accounts for the net change in total particles due to dissociation or recombination reactions:

$$\overline{M}_j(z) = \frac{\sum_i n_j^i(z) m^i}{n_{0,j}(p, T_j(z))} \tag{S6}$$

**Reaction rates** The chemical mechanism in Table S1 describes stoichiometric transformations of chemical species $i$ (of $N_s$ in total) for reaction $l$ (of $N_r$ in total) described by

$$\sum_{i=1}^{N_s} a_l^i X_i \rightarrow \sum_{i=1}^{N_s} b_l^i X_i \,, \tag{S7}$$

Here $X_i$ is the identity of species $i$ participating in the reaction and $a_l^i$ and $b_l^i$ are the stoichiometric coefficients. The reaction rate coefficients $k_l(T)$ at temperature $T$ for each reaction is described by its Arrhenius behavior, characterized by a rate constant $k_{0,l}$ and activation energy $E_{a,l}$

$$k_l(T) = k_{0,l} \exp\left(-\frac{E_{a,l}}{k_B T}\right) \tag{S8}$$

The chemical sources term of each species $R_j^i$, representing its net production rate per unit volume, is obtained by summation over all reactions:

$$R_j^i(z) = \sum_{l=1}^{N_r} \left[ (b_l^i - a_l^i) k_l(T_j(z)) \prod_{m=1}^{N_s} (n_j^m(z))^{a_l^m} \right] . \tag{S9}$$

**Transport equations** The diffusion rates $\Lambda_j^i$ [$\mathrm{m^{-3}s^{-1}}$] are given by

$$\begin{aligned}
&\Lambda_j^i \left(T_{j-1}(z), T_j(z), T_{j+1}(z), z\right) = \\
&\quad = \frac{4\pi}{A_j} n_{0,j}\left(p, T_{j-1}(z)\right) D_{j-1}\left(p, T_{j-1}(z)\right) \cdot \left\{ \frac{r_{j-1}(z)(\chi_{j-1}^i(z) - \chi_j^i(z))}{r_j(z) - r_{j-2}(z)} \right\} - \\
&- \frac{4\pi}{A_j} n_{0,j}\left(p, T_j\left(z\right)\right) D_j\left(p, T_j(z)\right) \cdot \left\{ \frac{r_{j-1}(z)(\chi_j^i(z) - \chi_{j-1}^i(z))}{r_j(z) - r_{j-2}(z)} + \frac{r_j(z)(\chi_j^i(z) - \chi_{j+1}^i(z))}{r_{j+1}(z) - r_{j-1}(z)} \right\} + \\
&\quad + \frac{4\pi}{A_j} n_{0,j}\left(p, T_{j+1}(z)\right) D_{j+1}\left(p, T_{j-1}(z)\right) \cdot \left\{ \frac{r_{j-1}(z)(\chi_{j-1}^i(z) - \chi_j^i(z))}{r_j(z) - r_{j-2}(z)} \right\} ,
\end{aligned} \tag{S10}$$

with $\chi_j^i$ the mole fractions of each species:

$$\chi_j^i(z) = \frac{n_j^i(z)}{n_{0,j}(p, T_j(z))}. \tag{S11}$$

Note that in the main text, $\Gamma_j^i$ [$\mathrm{m^{-2}s^{-1}}$] is expressed as a particle wall flux, while $\Lambda_j^i$ is expressed as a volumetric particle loss rate in [$\mathrm{m^{-3}s^{-1}}$]. The heat exchange equations in units of [$\mathrm{Wm^{-3}s^{-1}}$] are given by

$$\begin{aligned}
&Q_j\left(T_{j-1}(z), T_j(z), z\right) = P_{V,j}(p, z) + \\
&\quad + \frac{4\pi}{A_j} \left[ \lambda(T_{j-1}(z)) \frac{r_{j-1}(z)(T_{j-1}(z) - T_j(z))}{r_j - r_{j-2}} - \lambda(T_j(z)) \frac{r_j(T_j(z) - T_{j+1}(z))}{r_{j+1} - r_{j-1}} \right] ,
\end{aligned} \tag{S12}$$

where the final volume element $J$ includes a wall boundary condition (see main text):

$$Q_J\left(T_{J-1}(z), T_J(z), z\right) = P_{V,J}(p,z) + \\ + \frac{4\pi}{A_J}\left[\lambda(T_{J-1}(z))\frac{r_{J-1}(z)(T_{J-1}(z)-T_J(z))}{r_J - r_{J-2}(z)} - \right. \\ \left. - \frac{r_J(z)}{2}\left(\omega(T_J(z)-T_{env}) + \epsilon\sigma_{\mathrm{SB}}(T_J(z)^4 - T_{\mathrm{env}}^4)\right)\right]. \quad \text{(S13)}$$

The heat exchange equations $Q_j$ include power density $P_{V,j}(p,z)$, which is derived from an experimentally determined power density distribution function

$$P_{\mathrm{V}}(r,z) \equiv \rho_0 f(r) g(z) \quad \text{(S14)}$$

with $\rho_0$ the peak power density in $\mathrm{W/m^3}$ in the center of the plasma and $f(r)$ and $g(z)$ dimensionless functions of r and z. f(r) and g(z) are approximated by fitting to experimentally obtained radially resolved plasma emission intensity profiles of the 777 nm oxygen lines.

$$f(r) = \frac{1}{2}\exp\left(-\frac{(r-r_{\mathrm{offset}})^2}{2\sigma_r^2}\right) + \frac{1}{2}\exp\left(-\frac{(r+r_{\mathrm{offset}})^2}{2\sigma_r^2}\right) \text{ and} \quad \text{(S15)}$$

$$g(z) = \frac{1}{2}\exp\left(-\frac{(z-z_0-z_{\mathrm{offset}})^2}{2\sigma_z^2}\right) + \frac{1}{2}\exp\left(-\frac{(z-z_0+z_{\mathrm{offset}})^2}{2\sigma_z^2}\right). \quad \text{(S16)}$$

Here, double Gaussians are used with characteristic widths $\sigma_r$ and $\sigma_z$ and offsets $r_{\mathrm{offset}}$ and $z_{\mathrm{offset}}$ so that hollow profiles in r at low pressure and flat-topped distributions in z can be adequately accounted for. $z_0$ is the axial center position of the power deposition profile with respect to gas injection plane. Under proportionality of $n_e$ with emission intensity and Joule heating, the power density becomes

$$P_{V,j}(p,z) = \rho_0 2\pi g(z)\int_{r_{j-1}}^{r_j} f(r) r dr\ , \quad \text{(S17)}$$

where $\rho_0$ is obtained by normalization to the total absorbed power $P_{\mathrm{abs}}$

$$\rho_0 = \frac{P_{\mathrm{abs}}}{2\pi\int_0^{R_{\mathrm{tube}}} f(r) r dr \int_{-\infty}^{\infty} g(z) dz} \quad \text{(S18)}$$

Note that $P_{V,j}(p,z)$ becomes a function of z with an implicit pressure dependence in $\sigma_r$, $\sigma_z$, and their respective offsets.

The effective diffusion coefficient and effective heat conductivity are given, respectively, by

$$D_j\left(p, T_j(z)\right) = 1.0\times 10^{-4}\frac{T_j(z)^{3/2}}{p} + \frac{\nu_{T,j}}{Sc_T} \quad \text{(S19)}$$

and

$$\lambda_j(T_j(z)) = 2.5 \times 10^{-3} \frac{T_j(z)^{3/2}}{T_j(z) + 300} + C_{p,j}(z) n_{0,j} \frac{\nu_{T,j}}{Pr_T}\,, \tag{S20}$$

which are both discussed in more detail in the main text. The local heat capacity of the gas mixture $C_{p,j}(z) = \sum_i C^i_{p,j}(z)\chi^i_j$ [JK$^{-1}$particle$^{-1}$] is composed of the individual contributions of each species, $C^i_p$, which are individually calculated using the Shomate equation with coefficients obtained from the NASA Glenn library of thermodynamic properties[42] .

Energy transport rates from the core of the plasma in units of [J/s] are determined for a cylindrical test volume centered on the heat source, with a height $2\sigma_z(p)$ and radius $\sigma_r(p)$. The energy transport rate is determined separately for species diffusion $\Gamma_{E,D}$, species advection $\Gamma_{E,A}$ and heat conduction $\Gamma_{E,q}$ at the boundary between each volume element $j$ using

$$\Gamma_{E,D} = 2\pi r_j \int_{z_0-\sigma_z(p)}^{z_0+\sigma_z(p)} (\Gamma^i_{j,j+1}(z) \cdot H_i(z))dz, \tag{S21}$$

$$\Gamma_{E,A} = \pi r_j^2 v_j(z+\sigma_z(p))(n^i_j(z+\sigma_z(p)) \cdot H_i(T_j(z+\sigma_z(p)))) \tag{S22}$$

and

$$\Gamma_{E,q} = 2\pi r_j \int_{z_0-\sigma_z(p)}^{z_0+\sigma_z(p)} q_{j,j+1}(z)dz, \tag{S23}$$

where $\Gamma^i_{j,j+1}$ [m$^{-2}$s$^{-1}$] is the particle flux and $q_{j,j+1}$ [W/m$^2$] the heat flux density, both defined in the main text, and $H_j$ the enthalpy of species i in J/particle. To obtain the energy transport rates at the radius of $\sigma_r(p)$, interpolation between results for different $j$'s is applied.